Typhoon Nina and the August 1975 Flood over Central China

LONG YANG, MAOFENG LIU, AND JAMES A. SMITH

Department of Civil and Environmental Engineering, Princeton University, Princeton, New Jersey

FUQIANG TIAN

Department of Hydraulic Engineering, Tsinghua University, Beijing, China

ABSTRACT

The August 1975 flood in central China was one of the most destructive floods in history. Catastrophic flooding was the product of extreme rainfall from Typhoon Nina over a 3-day period from 5 to 7 August 1975. Despite the prominence of the August 1975 flood, relatively little is known about the evolution of rainfall responsible for the flood. Details of extreme rainfall and flooding for the August 1975 event in central China are examined based on empirical analyses of rainfall and streamflow measurements and based on downscaling simulations using the Weather Research and Forecasting (WRF) Model, driven by Twentieth Century Reanalysis (20CR) fields. Key hydrometeorological features of the flood event are placed in a climatological context through hydroclimatological analyses of 20CR fields. Results point to the complex evolution of rainfall over the 3-day period with distinctive periods of storm structure controlling rainfall distribution in the flood region. Blocking plays a central role in controlling anomalous storm motion of Typhoon Nina and extreme duration of heavy rainfall. Interaction of Typhoon Nina with a second tropical depression played a central role in creating a zone of anomalously large water vapor transport, a central feature of heavy rainfall during the critical storm period on 7 August. Analyses based on the quasigeostrophic omega equation identified the predominant role of warm air advection for synoptic-scale vertical motion. Back-trajectory analyses using a Lagrangian parcel tracking algorithm are used to assess and quantify water vapor transport for the flood. The analytical framework developed in this study is designed to improve hydrometeorological approaches for flood-control design.

1. Introduction

The August 1975 flood in central China (mainly southern Henan province and northern Hubei province, Fig. 1) was one of the most destructive floods in history (NOAA 2007). The maximum 6-h rainfall accumulation of 830 mm at Linzhuang station is comparable to the current world record (840 mm; Teegavarapu 2013). Maximum 1- and 3-day rainfall accumulations exceeded 1000 and 1600 mm, respectively, close to the storm center. Flooding from the torrential rainfall directly resulted in 26 000 fatalities and left approximately 10 million people without adequate shelter. Famine and disease in the postflood period resulted in approximately 100 000 additional fatalities (Hu and Luo 1992). The torrential rainfall and flooding inundated more than 1 million

hectares (2.5 million acres) of farmland throughout 29 counties and municipalities in southern Henan province. The August 1975 flood resulted in a financial loss of 10 billion CNY [about $6.7 billion (1975 U.S. dollars)] in property and crop damages (Wang 2006; Ding 2015; Ding and Zhang 2009).

Extreme rainfall and flooding for this event were associated with Supertyphoon Nina during a 3-day period from 5 to 7 August 1975. Typhoon Nina developed into a tropical storm from a tropical depression in the Philippine Sea on 31 July 1975 and moved to the northwest after its formation. It experienced explosive development during 1–2 August, with minimum sea level pressure dropping by 76 hPa and wind speed increasing by 35 m s^{-1}. Nina made its first landfall in Taiwan at 0600 UTC 3 August with a maximum wind speed of 35 m s^{-1} and then made a second landfall in Fujian province during the late hours on 3 August. It continued to move in a northwesterly direction after landfall and

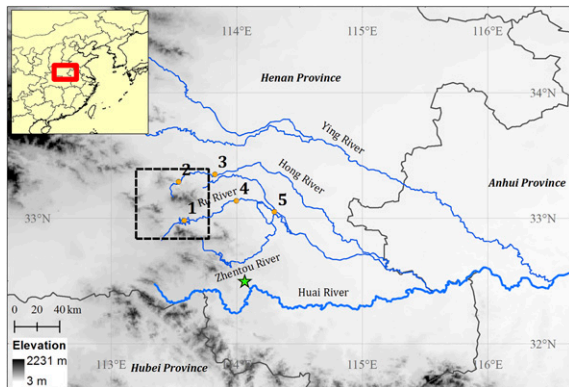*Corresponding author e-mail*: Long Yang, longyang@princeton.edu

FIG. 1. Location of central China (red box in the inset map) and regional map, including major tributaries (Ying River, Hong River, and Ru River) of the upper Huai River, as well as locations of key reservoirs and hydrological stations: 1) Banqiao, 2) Shimantan, 3) Yangzhuang, 4) Suiping, and 5) Suyahu. Black lines show province boundaries. Green star denotes the location of the sounding station. Topography (with a resolution of 1 km) is shaded in gray. Dotted box outlines the extreme rainfall region (see Fig. 3 for details).

FIG. 2. The envelope curve of the max rainfall–runoff floods over China. Red dots highlight floods induced by tropical cyclones [by following the procedures as in Villarini and Smith (2010), with the names of stream gauging stations labeled beside], while gray dots highlight floods with unidentified agents (mostly are because the specific dates of flood occurrence are unknown). Historical data were mainly collected from Li et al. (2013) and Luo and Shen (1987).

turned north on 5 August in Hubei province. Nina entered Henan province on 6 August and exhibited small net motion until its decay on 8 August.

Typhoon Nina ranks as the fourth deadliest tropical cyclone in world history (NOAA 2007). The devastating consequences of the August 1975 flood are closely linked to the cascading failures of dams, including two large dams, Banqiao and Shimantan, and 62 smaller reservoirs in the upper Huai River basin, Henan Province (see Fig. 1). Postflood studies showed that most of the dams that failed, especially Banqiao and Shimantan, were undersized relative to conventional design standards (see section 3 for more details). A historical tradition in China focused design of flood-control structures exclusively on direct observations and/or indirect postflood investigations of historical floods. Characterization of extreme floods is based on fitting available flood records to standard distribution functions used for flood frequency analysis (e.g., Pearson type-3 distribution; Lall and Beard 1982). The magnitudes of design floods are then determined by the corresponding points on the fitted curve with specified return periods. Errors in estimated design floods are most likely when flood records are limited or of poor quality (e.g., Dalrymple 1960; Gupta et al. 2014).

An important legacy of the August 1975 flood is that the design of flood-control structures in China began to incorporate estimation of probable maximum flood converted from probable maximum precipitation (PMP). The hydrometeorology approach for PMP analyses typically utilizes observed storms to assess extreme rainfall potential for specific regions. The August 1975 flood is an
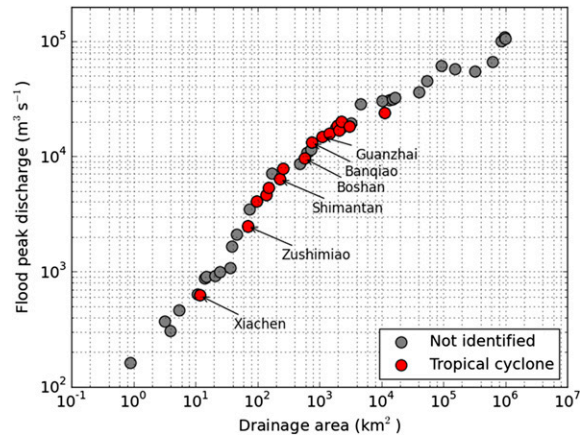
important candidate for PMP analyses because of its unprecedented severity. It has been "transferred" elsewhere in the country for PMP analyses (Luo and Shen 1987). It is not clear, however, how widely the August 1975 storms apply to assessments of extreme flood climatology in China. The contrasting geographic features of China result in large variations of the hydrometeorology of extreme rainfall. This study is motivated by the objective of improving the utility of the hydrometeorology approach in characterizing the upper-tail properties of extreme floods over China.

The August 1975 flood in central China plays a key role in shaping the distribution of extreme floods in China, as reflected in the envelope curve of the maximum rainfall–runoff floods over the country (Fig. 2; see also Table 1 for detailed statistics of the August 1975 flood). Tropical cyclones are important agents of extreme floods over China. Historical statistics show that most of the largest measured rainfall–runoff floods in China are located in typhoon-impacted basins or windward topographic regions (Costa 1987). Central China is located on the margin of the region experiencing frequent historical landfalling tropical cyclones (Wu et al. 2005). Therefore, a key issue for flood hazard characterization is to explore the anomalous features of Typhoon Nina that resulted in the unprecedented August 1975 flood over central China, the magnitude of which is also comparable to the largest world floods (Costa 1987). Nina is not an "unusual" typhoon in terms of its track and intensity, even though its track does not fall into the prevailing tropical cyclone tracks in the western

TABLE 1. List of max rainfall–runoff floods over China that occurred on 5–7 Aug 1975. See Fig. 2 for the positions on the envelope curve.

River	Station	Drainage area (km^2)	Peak discharge (m^3 s^{-1})	Return period (yr)
Ru	Xiachen	11.9	618	—
Shi	Zushimiao	71.2	2470	—
Gun	Shimantan	230	6280	200
Zhentou	Boshan	578	9550	>100
Ru	Banqiao	760	13000	600
Ganjiang	Guanzhai	1124	12100	>100

North Pacific basin (Wu et al. 2005). A broader motivation of this study is to explore the details of the August 1975 flood event associated with Typhoon Nina and assess the reasons why Typhoon Nina stands out as one of the deadliest tropical cyclones in the world.

The only detailed study of the August 1975 flood dates back to 1977 (Special Research Team for the "75.8" Heavy Rainstorm 1977a,b). That study, led by a team of Chinese researchers, qualitatively interpreted physical mechanisms of extreme rainfall and the large-scale synoptic environment based on limited in situ observations. We will revisit the mechanisms of extreme rainfall for the August 1975 flood based on downscaling simulations from the Weather Research and Forecasting (WRF) Model driven by Twentieth Century Reanalysis (20CR) fields. The 20CR fields provide great utility in reconstructing extreme historical storms (see, e.g., Chen and Hossain 2016), although the product is originally developed for climatological analyses. Smith and Baeck (2015) evaluated the utility of downscaling WRF simulations with 20CR fields in examining the 1927 Mississippi River flood. In this study, we will further evaluate the utility of WRF simulations forced by 20CR fields in examining historical flood events produced by tropical cyclones.

The paper is structured as follows. In section 2, we introduce datasets used in this study and configurations of the WRF Model. A summary of rainfall, flood magnitudes, and runoff for the August 1975 flood is presented in section 3. In section 4, we investigate physical mechanisms of extreme rainfall for this flood event based on WRF simulations. The large-scale environment and its hydroclimatological context for this flood event are examined based on the 20CR fields in in sections 5 and 6, respectively. A summary and conclusions are presented in section 7.

2. Data and methods

a. In situ observations, typhoon track, and reanalysis data

Daily rainfall records and time series of subhourly streamflow measurements for selected hydrological stations were manually extracted from the archived Chinese hydrological yearbook. Multiple rain gauges from the yearbook are located in the area of heavy rainfall (see Table 2 and Fig. 3), but the rain gauges from the yearbook are confined within a small region. We thus obtained additional rainfall measurements from a second rain gauge network (with daily rainfall), maintained by the China Meteorological Administration (CMA) [see Yang et al. (2013) for a previous study based on the network]. We rely on this network to derive spatial rainfall patterns of the flood event over a large region. We also utilized the University of Wyoming radiosonde archive for sounding observations during the flood period (http://weather.uwyo.edu/upperair/sounding.html; see Fig. 1 for the location of the sounding station).

TABLE 2. Daily and 3-day rainfall accumulation on 5–7 Aug 1975 for selected rain gauges (see Fig. 2 for spatial distribution). A "day" is defined as 0000–0000 UTC (0800–0800 LT).

| No.	Station name and location	5 Aug (mm)	6 Aug (mm)	7 Aug (mm)	3-day accumulation (mm)
1	Linzhuang (33.1°N, 113.6°E)	378	220	1005	1605
2	Xiachen (33.1°N, 113.6°E)	473	199	820	1492
3	Banqiao (33.0°N, 113.6°E)	448	190	784	1422
4	Huoshishan (33.0°N, 113.4°E)	334	125	666	1125
5	Shangdian (33.2°N, 113.5°E)	559	159	547	1265
6	Shizhuang (33.0°N, 113.5°E)	342	122	628	1092
7	Mayigou (32.9°N, 113.5°E)	263	164	639	1066
8	Taohuadian (33.0°N, 113.4°E)	267	144	642	1053
9	Baizhuang (33.3°N, 113.5°E)	180	177	628	984
10	Xiangheguan (33.1°N, 113.4°E)	243	92	633	968
11	Shuangmiao (33.1°N, 113.5°E)	292	117	532	941
12	Yuanmen (33.2°N, 113.5°E)	264	173	493	930
13	Shimantan (33.3°N, 113.5°E)	164	168	486	818
14	Jialou (32.9°N, 113.5°E)	143	187	344	675
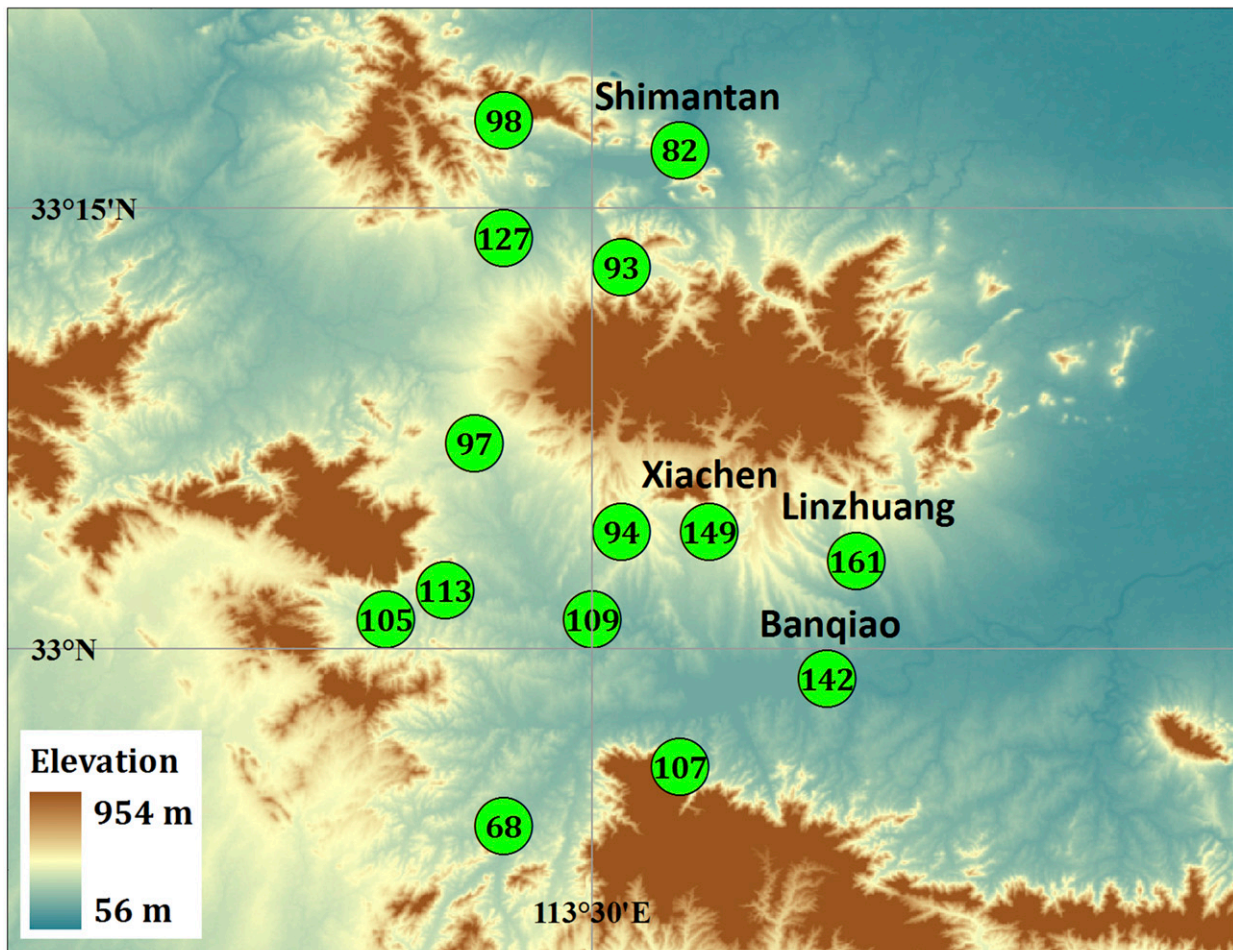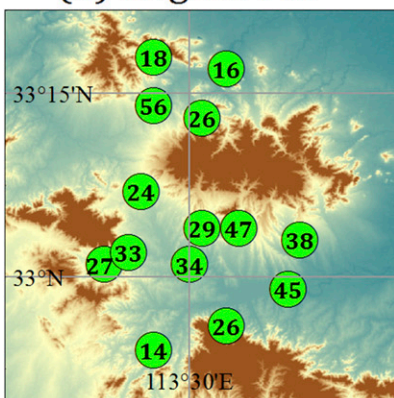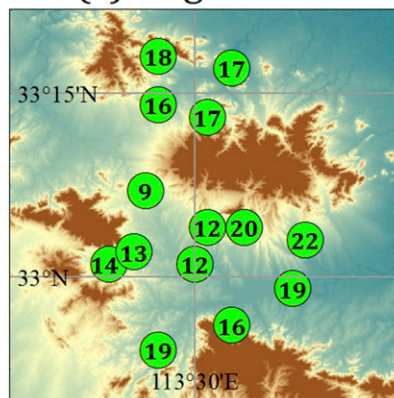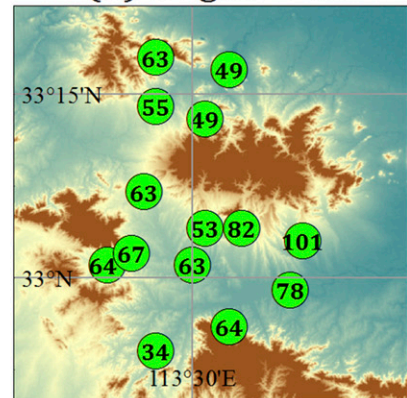
FIG. 3. (a) Three-day (5–7 Aug 1975) and (b)–(d) daily rainfall accumulation for selected rain gauges (listed in Table 1) over extreme rainfall region (see dotted line box in Fig. 1). Rainfall values (cm) are marked over the station symbol.
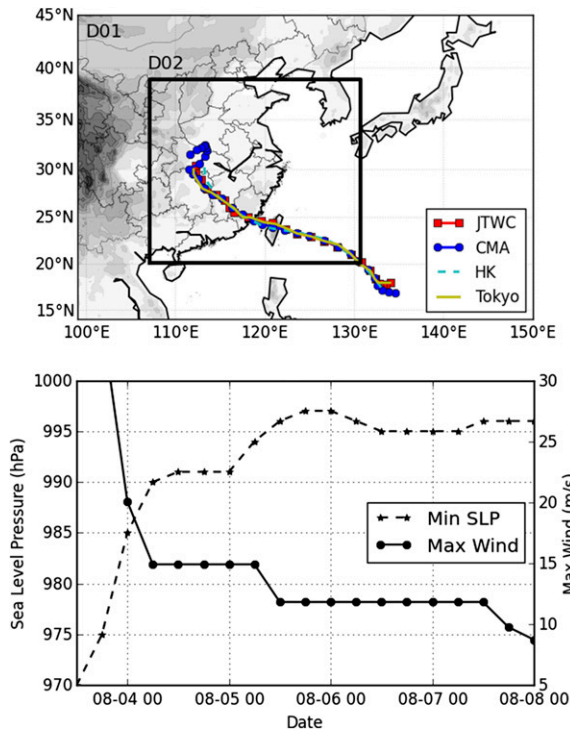
FIG. 4. (top) Two one-way nested WRF domains and topography (m; shaded) superimposed on the 6-hourly best tracks of Typhoon Nina from 0000 UTC 31 Jul to 0000 UTC 8 Aug 1975 by four different agencies (JTWC, CMA, HK, and Tokyo). (bottom) Time series of min sea level pressure (hPa) and max wind (m s^{-1}) from the CMA best track.

TABLE 3. Overview of WRF physics options.

Domain	D1	D2
Dimensions (x, y)	462×340	688×664
Grid size (km)	9	3
Time steps (s)	54	18
Output interval (h)	3	1
Cumulus scheme	None	
Microphysics scheme	WSM6	
Vertical layers	27	
Longwave radiation	RRTM scheme	
Shortwave radiation	Dudhia scheme	
Surface layer	Monin–Obukhov scheme	
Land surface	Noah land surface model	
Boundary layer	YSU	
Land use	MODIS 30 s	

spatial and temporal resolutions of the 20CR data are $2° \times 2°$ and 6 h, respectively.

b. Model configuration

The WRF Model is a fully compressible, nonhydrostatic, mesoscale model (Skamarock et al. 2008). The Advanced Research version of WRF (ARW), version 3.6, was used in this study. Two one-way nested domains were developed (as shown in Fig. 4). The horizontal grids are 462×340 and 688×664, with horizontal grid spacing of 9 and 3 km, respectively (Fig. 4). The vertical grids contain 39 sigma levels, and the upper boundary is set at 100 hPa. The time steps for the two domains are 54 and 18 s, respectively. Initial and boundary conditions for WRF simulation are based on the 20CR fields. Physics options used in the model are summarized in Table 3. We have tested the performance of different microphysics schemes [WRF single-moment 6-class microphysics scheme (WSM6) and WRF double-moment 6-class microphysics scheme (WDM6)], cumulus parameterizations (the Kain–Fritsch scheme, with or without the outer domain), and planetary boundary schemes [Yonsei University Scheme (YSU) and Mellor–Yamada–Janjić (MYJ)]. The current model configurations provide the best evaluation against ground-based observation (specifically for this event). The simulation is initiated at 1200 UTC 3 August and run until 0000 UTC 8 August 1975. The output interval is 1 h for the inner domain. In addition to downscaled WRF simulations, we also identify moisture sources feeding this flood event based on the Lagrangian Analysis Tool [LAGRANTO; see Sprenger and Wernli (2015) for details] using the WRF-simulated fields.

The best track data for Typhoon Nina were obtained from the International Best Track Archive for Climate Stewardship (IBTrACS; Schreck et al. 2013; Knapp et al. 2010). This dataset includes the locations of the storm circulation center and its intensity (including maximum wind and minimum sea level pressure) at 6-h time interval. Figure 4 shows the tracks of Nina from four different agencies in the IBTrACS archive [CMA, Joint Typhoon Warning Center (JTWC), Hong Kong (HK), and Tokyo Typhoon Center (Tokyo)] are broadly consistent (Fig. 4). Typhoon track data from CMA extend 2 days after 6 August, unlike track data from the other three sources, but are quite similar to the other agencies before 6 August. We use the best track from CMA in the following analyses (also see Fig. 4 for the time series of estimated intensity), because Nina exerted significant impacts over central China after 6 August.

We utilize the 20CR, version 2, data (6-hourly ensemble mean; Compo et al. 2011) for initial and boundary conditions of WRF simulations and for hydro-climatological analyses that are used to assess anomalies in the structure and evolution of Typhoon Nina. The

3. Rainfall and flood summary

Heavy rainfall from Typhoon Nina extended over a 3-day period from 5 through 7 August 1975. The largest

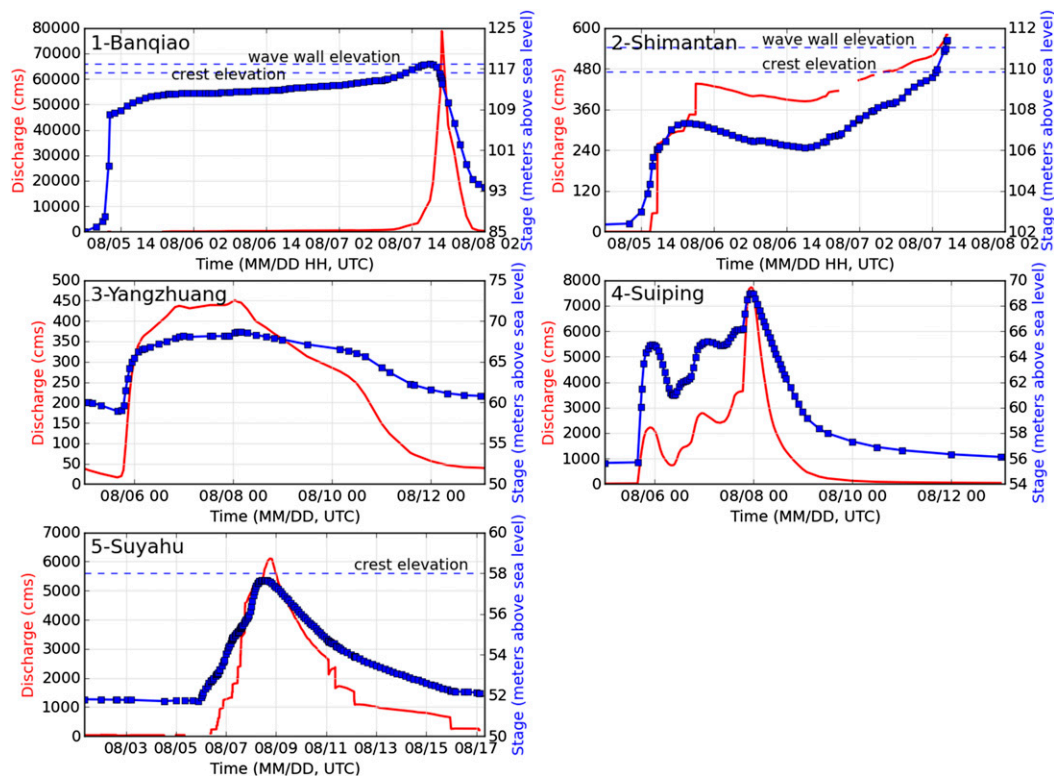FIG. 5. Time series of water level (m; blue squares) and discharge (m³ s⁻¹; red line) for selected hydrological stations (see Fig. 1 for locations). Blue dotted lines highlight critical levels for the Banqiao, Shimantan, and Suyahu Dams.

3-day rainfall accumulation was 1605 mm at the Linzhuang station (Table 2, Fig. 3), which comprised 378 mm on 5 August, 220 mm on 6 August, and 1005 mm on 7 August. Rainfall accumulations for the 3-day period exceeded 1000 mm at eight stations (Table 2, Fig. 3). The rain gauge station at Xiachen reported 1492 mm (second-largest value among all rain gauges) for the 3-day period and also had the second-largest daily accumulation of 820 mm (see discussion below about the record flood peak at Xiachen).

The rain gauge station at Banqiao reported the third-largest 3-day total, 1422 mm, with 784 mm on 7 August. Daily rainfall accumulations on 7 August exceeded 500 mm for 11 stations. The largest daily and 3-day rainfall accumulations were located over and immediately north of the Banqiao Reservoir (Fig. 3). There was heavy rainfall around Banqiao Reservoir on 5 August, but rainfall over the same area on 7 August was unprecedented. Rain gauge observations support the observation that the most exceptional consequences of Nina were due to heavy rainfall in a relatively small area (around 100 km²) around Banqiao Reservoir on 7 August.

Rainfall measurements in the area around the Shimantan Reservoir (Fig. 3) were only slightly smaller than those in the Banqiao area. The 3-day rainfall accumulation at

Shangdian, immediately upstream of the Shimantan Reservoir, reached 1265 mm. Shangdian had the largest daily rainfall of any rain gauge station on 5 August, 560 mm, slightly larger than the 547 mm at Shangdian on 7 August.

The water level of the Banqiao Reservoir (see Fig. 1 for location) began to rise early on 5 August in response to the intense rainfall and reached an elevation of 107.9 m MSL at the end of the day (Fig. 5). The top of the flood-control pool is at an elevation of 110.9 m for Banqiao Reservoir. On 6 August, the water level continued to rise due to preceding rainfall and a sequence of heavy rain pulses; the water level reached 112.9 m by 2300 local time (LT; 1500 UTC). Although all spillways were fully operational, inflow continued to raise the water level to higher elevations. On 7 August, the water level reached 117.9 m, 0.3 m higher than the dam-crest elevation. The peak discharge of the inflow was 13 000 m³ s⁻¹, nearly 8 times larger than the maximum discharge capacity of the spillway (1700 m³ s⁻¹).

The unprecedented inflow and inadequate discharge capacity resulted in the collapse of the main section of Banqiao Dam in the early morning on 8 August (at around 0100 LT; see Yang 2005). As recalled by survivors, the sky cleared at around 0100 LT (1700 UTC), and

someone yelled "the water level is going down! The flood is retreating!" Just a few seconds later, it "sounded like the sky was collapsing and the earth was cracking" (Fish 2013). The dam-break flood, with a peak discharge of $78\,100\,\text{m}^3\,\text{s}^{-1}$, formed a wall of water 5–9 m high and 12–15 km wide (Dai 1998). The flood wave rushed downstream with an estimated velocity of 30–$50\,\text{km}\,\text{h}^{-1}$ (Dai 1998) and arrived at Suiping (the downstream station of Banqiao) at 1800 UTC 8 August (Fig. 5). Postflood studies showed that 701 million m^3 of water were transported downstream within 6 h, inundating an area of $11\,250\,\text{km}^2$ over southern Henan Province. By the evening on 9 August, floods reached Anhui Province, which is roughly 250 km away from the reservoir (Dai 1998).

A second large dam, the Shimantan Dam, failed because of overtopping (Yang 2005; Wang 2006). The peak discharge of the dam-break flood for Shimantan Dam was $30\,000\,\text{m}^3\,\text{s}^{-1}$ (Wang 2005, 2006), with a maximum water level of 111.40 m (0.35 m above the dam-crest elevation; Fig. 5). The peak discharge of inflow to the Shimantan Reservoir was $6280\,\text{m}^3\,\text{s}^{-1}$, and 120 million m^3 of water was discharged from the Shimantan Reservoir within 5 h.

The collapse of the Banqiao and Shimantan Dams initiated cascading failures of 62 smaller dams in southern Henan Province. Major floods occurred over the tributaries of the upper Huai River, including the Hong, Ru, and Ying Rivers (see Fig. 1). The Suyahu Dam is the largest dam in the region, with a capacity of 1600 million m^3. The water level of the Suyahu Dam rose sharply on 7 August in response to intense rainfall, and even more rapidly on 9 August in response to the dam-break flood from Banqiao (Fig. 5). Water level crested only 0.34 m away from its maximum elevation of 58 m.

The August 1975 flood over central China plays an important role in determining the upper tail of flood peaks in China, as reflected in the envelope curve of flood peaks for the country [Fig. 2, Table 1; see also Luo and Shen (1987)]. The most extreme flood peak measurement was from the Ru River above Banqiao Reservoir. The peak discharge was approximately $13\,000\,\text{m}^3\,\text{s}^{-1}$ at a drainage area of $760\,\text{km}^2$ (unit discharge of $17.1\,\text{m}^3\,\text{s}^{-1}\,\text{km}^{-2}$, which is discharge divided by total drainage area, same as below). The magnitude of the peak discharge was significantly larger than the estimated 1000-yr flood magnitude (approximately $4000\,\text{m}^3\,\text{s}^{-1}$), which was used for the design of Banqiao Dam in the early 1950s. Postevent investigation and estimation show that the $13\,000\,\text{m}^3\,\text{s}^{-1}$ peak is approximately a 600-yr flood (Wang 2006), which indicates that the reservoir was greatly undersized.

The Xiachen hydrologic station, located in the upper Ru River, observed a peak discharge of $618\,\text{m}^3\,\text{s}^{-1}$
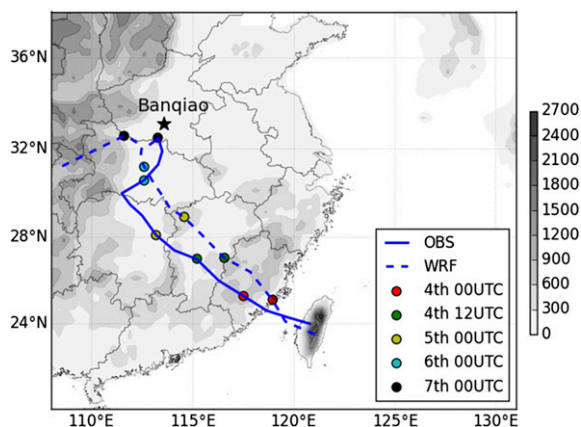

FIG. 6. Comparison of Nina's track: best track from CMA [observed (OBS)] and simulated track from the WRF Model, with positions of circulation center plotted every 6 h. The colored points highlight the position of circulation center at different times. Topography is shaded in gray (m).

(with a unit discharge of $52\,\text{m}^3\,\text{s}^{-1}\,\text{km}^{-2}$). The rain gauge of Xiachen is just north of Banqiao Reservoir and observed the second-largest rainfall accumulation during the 3-day period. The return period of the original design flood for Shimantan reservoir, which nominally had a return interval of 500 years, was barely 10 years according to updated investigations in the 1980s (Wang 2006). Nationwide assessments and checks on flood-control standards of large reservoirs were carried out after the destructive 1975 flood event over Henan Province (Fu 2005).

4. Model-based analyses of rainfall mechanisms

a. Comparison of model simulation with observations

In this section we compare WRF Model simulations with observations, focusing on the performance of the model in reproducing the evolution of Typhoon Nina, including track and intensity, as well as the spatiotemporal pattern of extreme rainfall over Henan Province on 5–7 August 1975.

The model generally captures the motion of Nina, although the simulated track (based on the location of lowest sea level pressure) is shifted north of the best track (Fig. 6). On 5 August, the circulation center is about 500 km away from the flood region; thus, the departure of the simulated track does not significantly affect the simulated rainfall field on that day (as discussed below). As Nina approached the flood region on 6 August, the simulated circulation center was close to the best track (within 50 km). On 7 August, Nina had weakened significantly, making it difficult to precisely determine the location of minimum
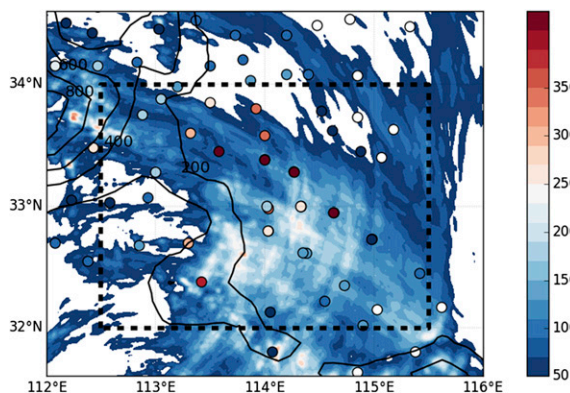
FIG. 7. Comparisons of WRF-simulated rainfall fields (mm; shaded) with observations (mm; scatterplots) for 3-day rainfall accumulation on 5–7 Aug. Black lines denote the contours of topography over the region. Dotted line outlines the "defined" storm region (32°–34°N, 112.5°–115.5°E).

FIG. 8. As in Fig. 7, but for daily rainfall accumulation on 5 Aug 1975 (at 1200–1200 UTC, which is 2000–2000 LT).

sea level pressure. The small net storm motion after 6 August, a critical element of extreme rainfall production in Henan Province, is accurately reproduced in the model.

Simulated rainfall fields from the 3-km domain are compared against daily rainfall observations based on the CMA rain gauge network. A dense network of rain gauges enables us to derive spatial patterns of extreme rainfall for the August 1975 flood. Extreme rainfall is principally distributed over southern Henan Province around the 32°–34°N and 112.5°–115.5°E region (defined as "storm region" in this study). Comparisons of 3-day rainfall accumulation (from 0000 UTC 5 August to 0000 UTC 8 August; see Fig. 7) show that the WRF Model simulations capture elements of the structure of extreme rainfall, but underestimate rainfall totals (Fig. 7). The simulated maximum daily rainfall accumulation on 5–7 August is approximately 350 mm, while several rain gauges observed total rainfall exceeding 1000 mm within the same period (Table 2). The underestimation could be partially due to the inability of a 3-km-resolution simulation in resolving convective rainfall in complex terrain (Knutson et al. 2013; Davis et al. 2008a; Li et al. 2014) and deficiencies of model physics (Khain et al. 2016; Jankov et al. 2005; Li et al. 2014), as well as the absence of data assimilation procedure in the simulations (e.g., Zhang et al. 2013). We will principally use the simulations to provide insights on the changing structure of rainfall over the 3-day period and to examine elements of the storm environment.

Daily rainfall accumulations on 5–7 August are further compared in Figs. 8–10, respectively. The major rainbands were oriented in an east–west direction on 5 August and shifted toward a northwest–southeast orientation on 6 August, reflecting the evolution of the
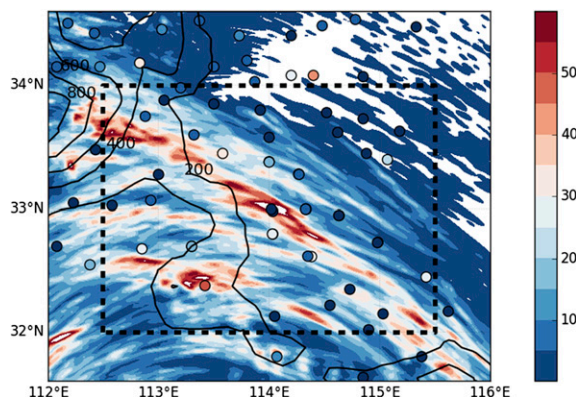
vortex structure along the track of Nina. On 7 August, the dominant rainband was nearly north–south in orientation, with extreme rainfall located in the right-rear quadrant of the storm circulation.

Water vapor was principally transported to the storm region at vertical levels below 800 hPa, and low-level water vapor transport intensified from 5 to 7 August (Fig. 11). The mixing ratios at 850 hPa were greater than $0.015 \, \mathrm{kg \, kg^{-1}}$ during the 3-day period, with a maximum value of $0.017 \, \mathrm{kg \, kg^{-1}}$ attained on 7 August. Low-level transport of moisture is an important feature for the August 1975 flood over central China, as will be elaborated below. The WRF simulation captures key elements of timing of heavy rainfall and spatial structure of rainfall during the 3-day period, despite the discrepancies mentioned above.

b. Rainfall structure and evolution

We utilize WRF simulations to examine the temporal structure of extreme rainfall during the August 1975 flood. Time series of spatially averaged hourly rain rate,
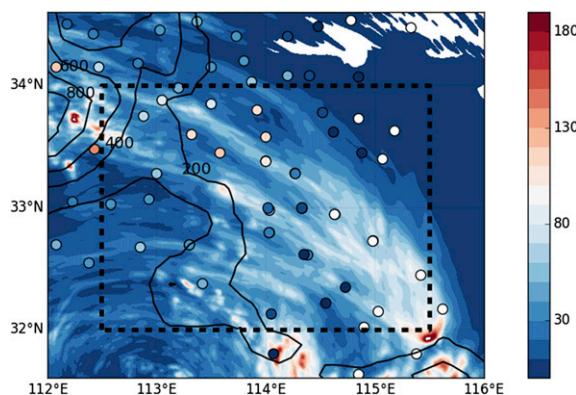

FIG. 9. As in Fig. 7, but for daily rainfall accumulation on 6 Aug 1975 (at 1200–1200 UTC, which is 2000–2000 LT).
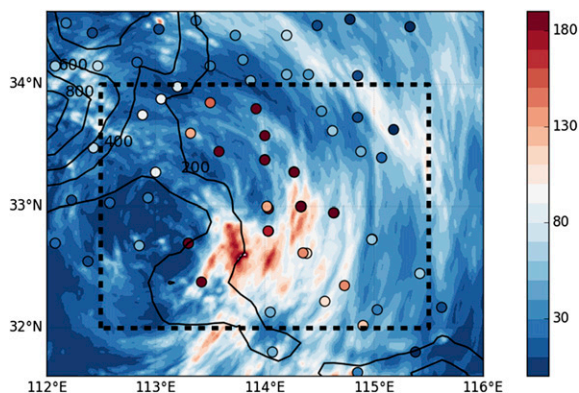
FIG. 10. As in Fig. 7, but for daily rainfall accumulation on 7 Aug 1975 (at 1200–1200 UTC, which is 2000–2000 LT).

precipitable water (from 1000 to 275 hPa), and horizontal water vapor convergence (from 1000 to 275 hPa) for the storm region (dotted line box in Fig. 7) illustrate evolution of rainfall and storm environment over the period of heavy rainfall (Fig. 12a). The largest values of water vapor convergence and precipitable water change occurred on the first day of heavy rainfall, 5 August. Large values of water vapor convergence on 5 August resulted in rapid moistening of the atmosphere and the onset of heavy rainfall, with rainfall lagging water vapor convergence. From approximately 1800 UTC 5 August to 0000 UTC 8 August, the time series of basin-averaged rainfall rate varies directly with water vapor convergence.

Daily integrals of the water-balance components (Fig. 12b) highlight the moistening of the atmosphere on 4 and 5 August, followed by 2 days of convergence-driven rainfall production. Precipitation efficiency, defined as total precipitation divided by net water vapor supply [including contributions from surface evaporation, decrease of precipitable water and horizontal water convergence; see Gao and Li (2008) and Sui et al. (2007) for more details about the definition] is close to 100% for both 6 and 7 August. High precipitation efficiency was accompanied by extreme rainfall intensity (e.g., Huang et al. 2014). Rainfall accumulations on 7 August exceeded 500 mm for all listed stations in Table 2.

We examine in detail three rainfall episodes on 5–7 August based on the time series of hourly rain rates. The selected rainfall periods are at 0900–1200 UTC 5 August, 1300–1600 UTC 6 August, and 1500–1800 UTC 7 August. We examine contrasting ingredients for extreme rainfall during the August 1975 flood by focusing specifically on the selected rainfall episodes.

1) 5 AUGUST

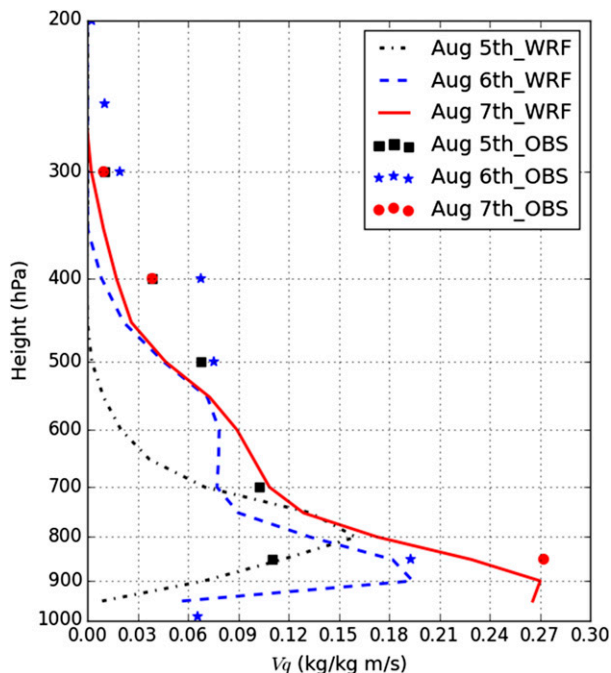At 0900 UTC 5 August (Fig. 13), heavy rainfall was concentrated in outer rainbands approximately 460–

FIG. 11. Comparisons of WRF-simulated vertical profiles of water vapor flux with sounding observations (see Fig. 1 for location) at 0000 UTC 5 Aug, 0000 UTC 6 Aug, and 0000 UTC 7 Aug 1975.

510 km from the circulation center of Nina and the outer band of cyclonic circulation interacted with a weak warm front moving from east to west. A strong east–west-oriented convergence zone formed along the latitude of
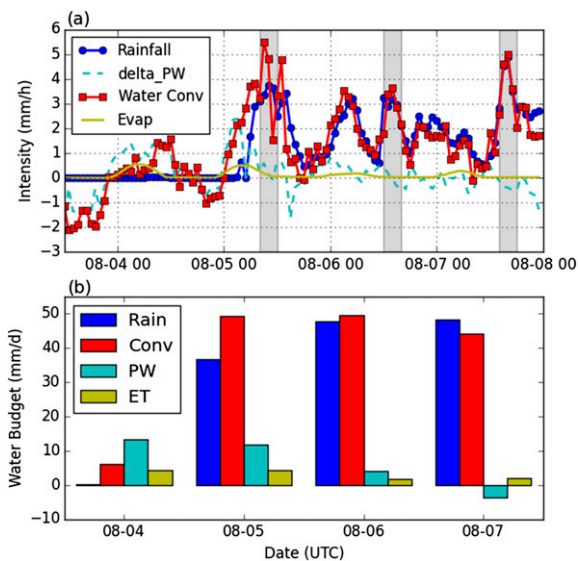

FIG. 12. (a) Time series of hourly rain rate, changes of precipitable water (delta_PW), water convergence (Water Conv), and surface evaporation rate (Evap) over the storm region (see the black dotted line box in Fig. 7). Gray-shaded region denotes three main rainfall episodes. (b) Daily integrals of rainfall, changes of precipitation water (PW), water convergence (Conv), and evaporation (ET) over the storm region.
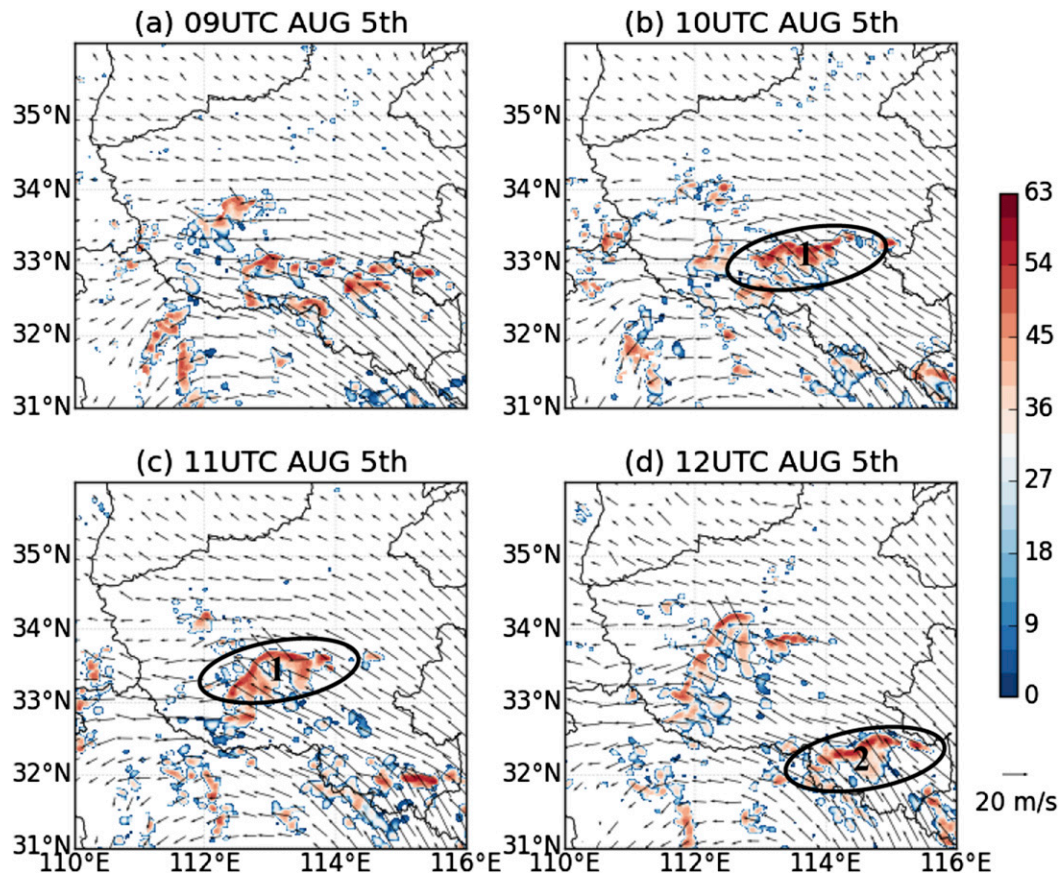
FIG. 13. WRF-simulated reflectivity (at 850 hPa; dBZ; shaded) and steering-level (at 850 hPa) wind (m s^{-1}; vectors) at (a) 0900, (b) 1000, (c) 1100, and (d) 1200 UTC 5 Aug 1975. Black lines represent provincial boundaries. The ellipses (labeled as "1" and "2") represent the envelopes of storm cells.

33°N. A cluster of storm cells (with radar reflectivity exceeding 40 dBZ) was generated along the convergence zone. The storm cells moved slowly to the northwest under the cyclonic circulation of Nina. Storm cells merged into a larger band over the region where Linzhuang station is located (around 33°N, 113°E; identified as storm cell 1 in Fig. 13b) at 1000 UTC 5 August. The intensification of convection was observed during the merger process, with maximum reflectivity values exceeding 60 dBZ. The height of maximum reflectivity (about 65 dBZ) was approximately 6 km. Echo-top height, defined by the maximum height with reflectivity larger than 18 dBZ (e.g., Hamada et al. 2015; Yang et al. 2016), approached 13 km above the surface, indicating deep convection in these areas (figure not shown). Merged storm entities tend to exhibit increased storm depth and heavier rainfall (e.g., Fu and Guo 2012; Ping et al. 2014; Changnon et al. 1976).

Domain-averaged surface rain rate attained its peak at 1000 UTC 5 August, and the rainfall peak was sustained for the following 2 h into 1200 UTC 5 August. The main band of cells continued to move to the northwest after 1100 UTC 5 August (Fig. 13c). Another storm element (identified as storm cell 2 in Fig. 13d) merged from smaller storm cells and moved into the storm region along the similar path of storm cell 1. The second storm element sustained peak rain rates after reaching peak in terms of domain-averaged rainfall. The structure and evolution of outer rainbands on 5 August played an important role in priming the region (via moistening the atmosphere and surface soil) for extreme flooding in the subsequent days.

2) 6 AUGUST

The storm center of Nina approached the boundary of Henan Province on 6 August, and the storm system entered a critical period characterized by a small net motion (Fig. 14). Multiple pulses of heavy rainfall over the flood region can be identified on 6 August. We focus on the period from 1300 to 1600 UTC for detailed analyses.
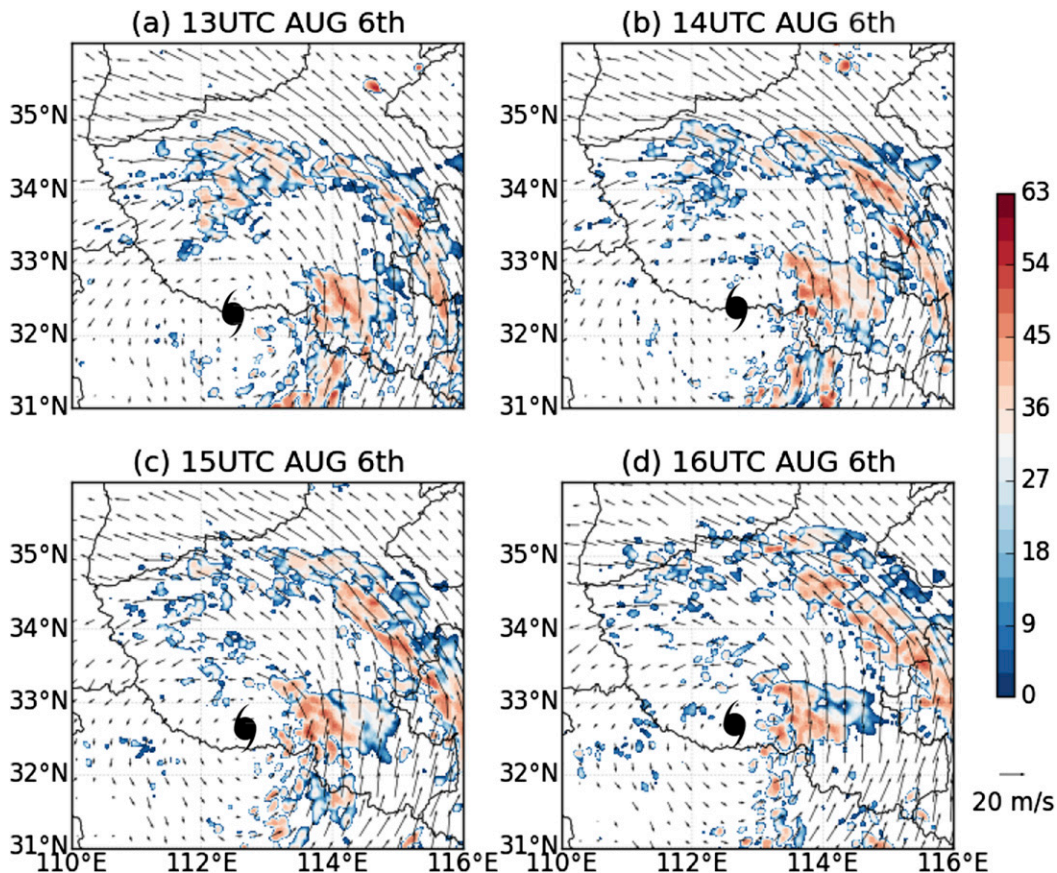
FIG. 14. As in Fig. 13, but for results at (a) 1300, (b) 1400, (c) 1500, and (d) 1600 UTC 6 Aug 1975. The typhoon symbols represent eye locations of Typhoon Nina (represented by min sea level pressure).

Rainfall on 6 August in the flood region was associated with inner and outer rainbands that were concentrated in the right quadrant of the storm (Fig. 14). A right-rear quadrant distribution of rainfall is observed for rainfall on 6–7 August (Figs. 9, 10). Previous studies have pointed out that asymmetric distribution of rainfall from tropical cyclones is linked to the role of vertical wind shear (Corbosiero and Molinari 2003, 2002; Gao et al. 2009). We calculated the environmental wind shear of Nina based on the mean wind difference between 200 and 850 hPa averaged over a 200–800 km annulus from the storm center (Fig. 15a; see, e.g., Chen et al. 2006; Gao et al. 2009). A striking feature is that the wind shear vectors consistently pointed toward the south or southeast during the life cycle of Nina (Fig. 15a). The wind shear gradually increased and exceeded $14\,\mathrm{m\,s^{-1}}$ during the main rainfall episodes on 6–7 August.

The distribution of rainfall in the right-rear quadrant of the storm is associated with the downshear rainfall concentration induced by wind shear (Corbosiero and Molinari 2003, 2002; Gao et al. 2009). The rainfall asymmetry is further explored using 500-hPa vertical mass flux

defined as the product of air density and vertical velocity (Davis et al. 2008b). The total mass flux is integrated over the encircled area 400 km from the storm center (i.e., 400 km is the radius of the circle; same as below). Upshear and downshear mass flux are integrated over the semicircle relative to shear vector. The total mass flux is dominated by mass flux in the downshear side, highlighting the downshear convective asymmetry (see Fig. 15a). Local vortex shear (400 km from the storm center) and environmental shear (200–800 km) from 850 to 500 hPa are much smaller than the "deep" shear (850–200 hPa, Fig. 15b), which helps Nina maintain its vortex structure after landfall.

Typhoon Nina experienced profound changes in storm environment after leaving the tropics and making landfall. The interaction between tropical cyclones and midlatitude baroclinic environment can trigger extratropical transition, which is one of the key elements of extreme rainfall produced by landfalling tropical cyclones in many settings (e.g., Atallah and Bosart 2003; Colle 2003; Jones et al. 2003; Atallah et al. 2007; Liu and Smith 2016). We examine extratropical transition for Typhoon Nina using the cyclone phase space (CPS)
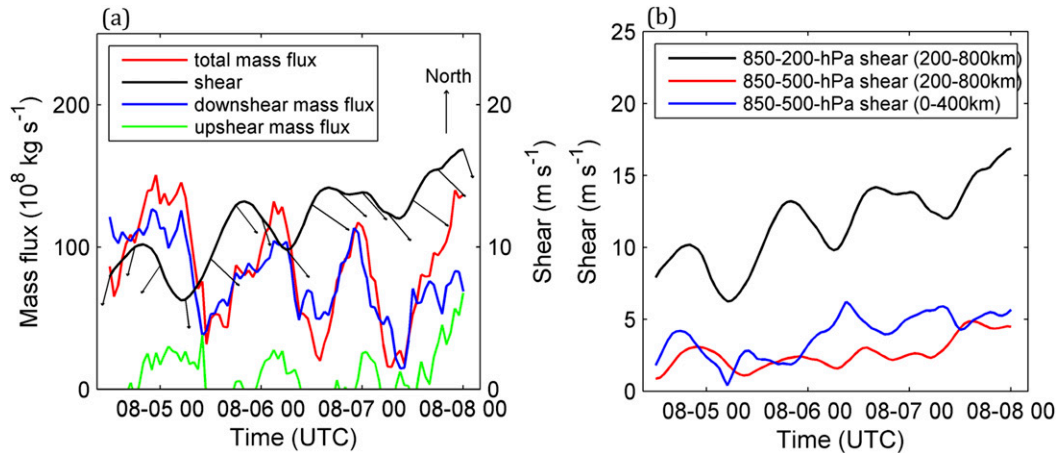
FIG. 15. Time series of (a) mass flux at 500 hPa in a region of 400 km from storm center and environmental vertical wind shear from 850 to 200 hPa (i.e., deep shear) and (b) vertical wind shear from 850 to 500 hPa and also from 850 to 200 hPa (both local vortex and environmental shear) of Nina from 1200 UTC 4 Aug to 0000 UTC 8 Aug 1975. The upshear and downshear mass flux are also presented. Black arrows indicate the directions of vertical wind shear.

method (for more details, see Evans and Hart 2003; Hart 2003) and simulated fields from the outer domain. The CPS analyses indicate that Nina did not undergo extratropical transition and retained its symmetric structure and weak warm core or cold core in low levels over its life cycle (Fig. 16). Extratropical transition is thus not a factor in the production of heavy rainfall from Nina.

3) 7 AUGUST

The small net storm motion continued into 7 August. Compared to the positions of the storm center on 6 August, Typhoon Nina moved into southwestern Henan Province at 0000 UTC 7 August and remained

nearly stationary until its decay on 8 August (Fig. 17). The intensity of Nina continued to weaken on 7 August, with maximum wind speeds reduced to $10 \, m \, s^{-1}$ and minimum sea level pressure increased to 995 hPa. Rainfall intensity, however, was even heavier on 7 August than the previous 2 days. A strong rain pulse occurred at around 1600 UTC 7 August (0000 LT 8 August). The rain pulse produced the largest instantaneous rain rate during the entire flood period on 5–7 August (Fig. 7) and was a principal cause of the collapse of the Banqiao Dam.

The increased rainfall intensity on 7 August is tied to exceptional transport of water vapor into the storm
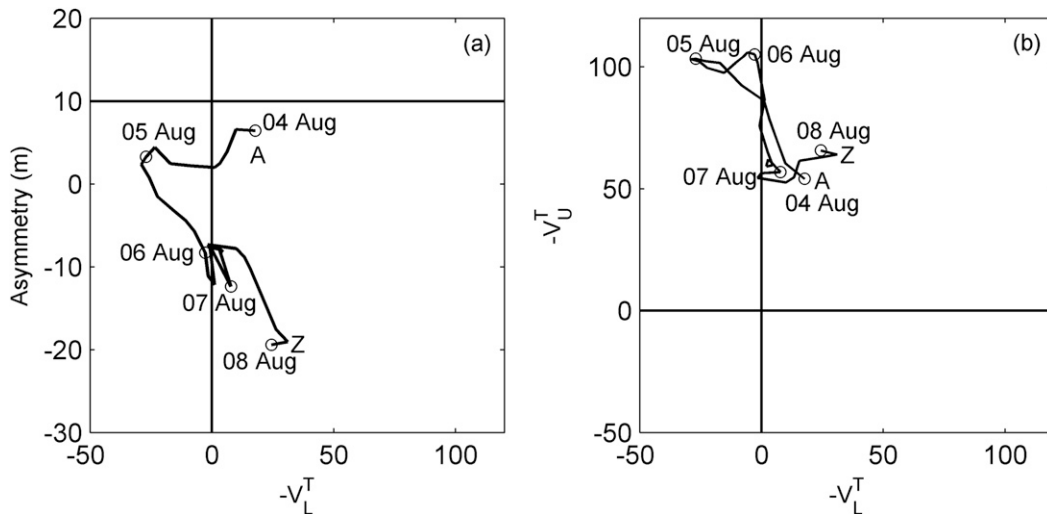

FIG. 16. The cyclone phase space diagram of (a) thickness asymmetry B (m) vs 900–600-hPa thermal wind $-V_L^T$ and (b) 600–300-hPa thermal wind $-V_U^T$ vs 900–600-hPa thermal wind.
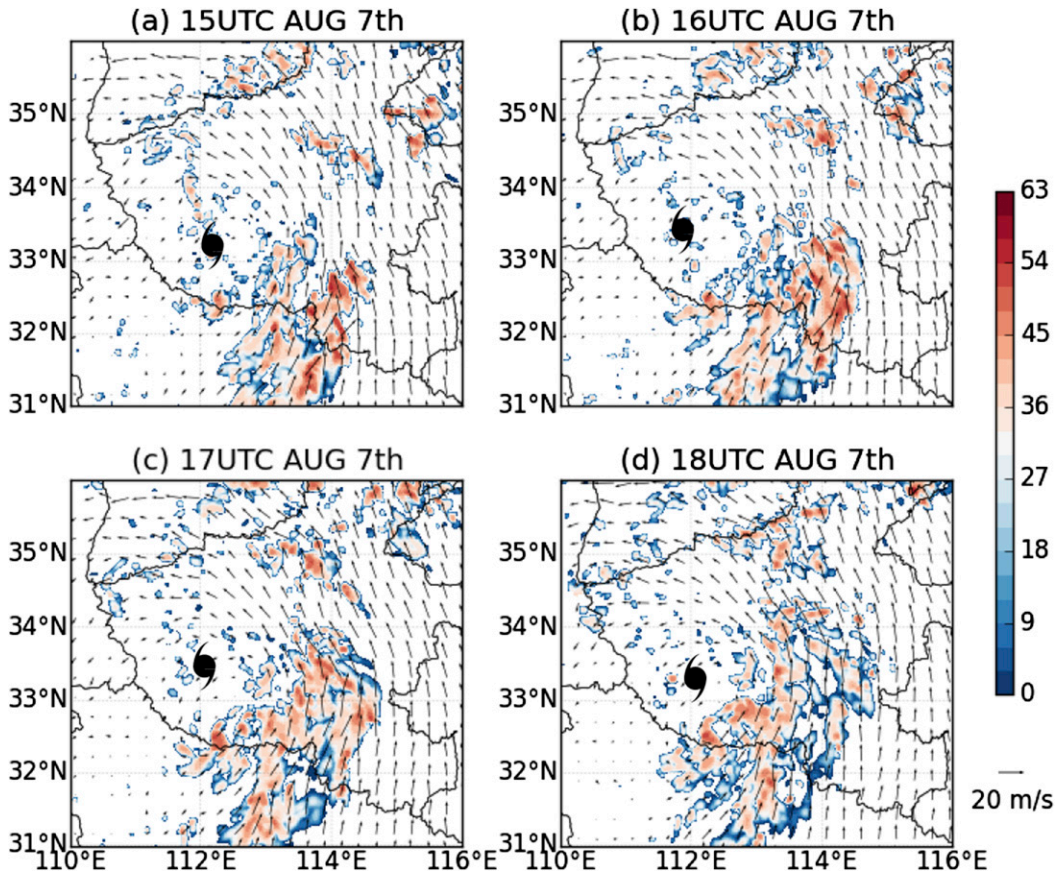
FIG. 17. As in Fig. 14, but for results at (a) 1500, (b) 1600, (c) 1700, and (d) 1800 UTC 7 Aug 1975.

region. The "multiple rain bands" on 6 August in the storm region were replaced on 7 August by a single organized major rainband with north-to-south orientation. This rainband showed little movement and produced extreme rainfall. The simulated maximum reflectivity approached 65 dBZ, indicating strong convection within the embedded storm cells. Slow motion and exceptional water vapor transport to the storm system are the main players for extreme rainfall on 7 August. In the following section, we will examine large-scale controls of water vapor transport.

Previous studies also identified complex topography as an important player in the extreme rainfall during the August 1975 flood (Special Research Team for the "75.8" Heavy Rainstorm 1977b; Ding and Zhang 2009). As can be seen in Fig. 3, extreme rainfall stations are surrounded by regions with topographic transitions. Previous studies also identified the role of complex topography in producing asymmetric rainfall structure of typhoon (e.g., Xie and Zhang 2012; Gao et al. 2009). Future research will examine topographic controls of extreme rainfall for the August 1975 flood.

5. Large-scale environment

a. Synoptic forcing

We diagnose the synoptic-scale vertical forcing using the quasigeostrophic (QG) omega equation (see, e.g., Trenberth 1978) based on the 20CR data. The QG omega equation takes the form as

$$\left(\nabla_p^2 + \frac{f_0^2}{\sigma}\frac{\partial^2}{\partial p^2}\right)\omega = -\frac{f_0}{\sigma}\frac{\partial}{\partial p}[-\mathbf{V}_g \cdot \nabla_p(\zeta_g + f)] \quad \text{(term } A\text{)}$$
$$+ \frac{R}{\sigma p}[-\nabla_p^2(-\mathbf{V}_g \cdot \nabla_p T)], \quad (1)$$
$$\text{(term } B\text{)}$$

where ∇_p is the gradient on a pressure surface (m^{-1}), ∇_p^2 is a Laplacian operator on a pressure surface (m^{-2}), f is the Coriolis parameter (s^{-1}; $f_0 = 1.0 \times 10^{-4}$ s^{-1}), σ is the static stability (assumed constant at 2.0×10^{-6} m^2 Pa^{-2} s^{-2}), p is the pressure (Pa), $\mathbf{V}g$ is the geostrophic wind (m s^{-1}), R is the gas constant for dry air ($R = 287$ J K^{-1} kg^1), T is the temperature (K), and ζ_g is the geostrophic relative vorticity (s^{-1}). The first term (term A) on the right-hand

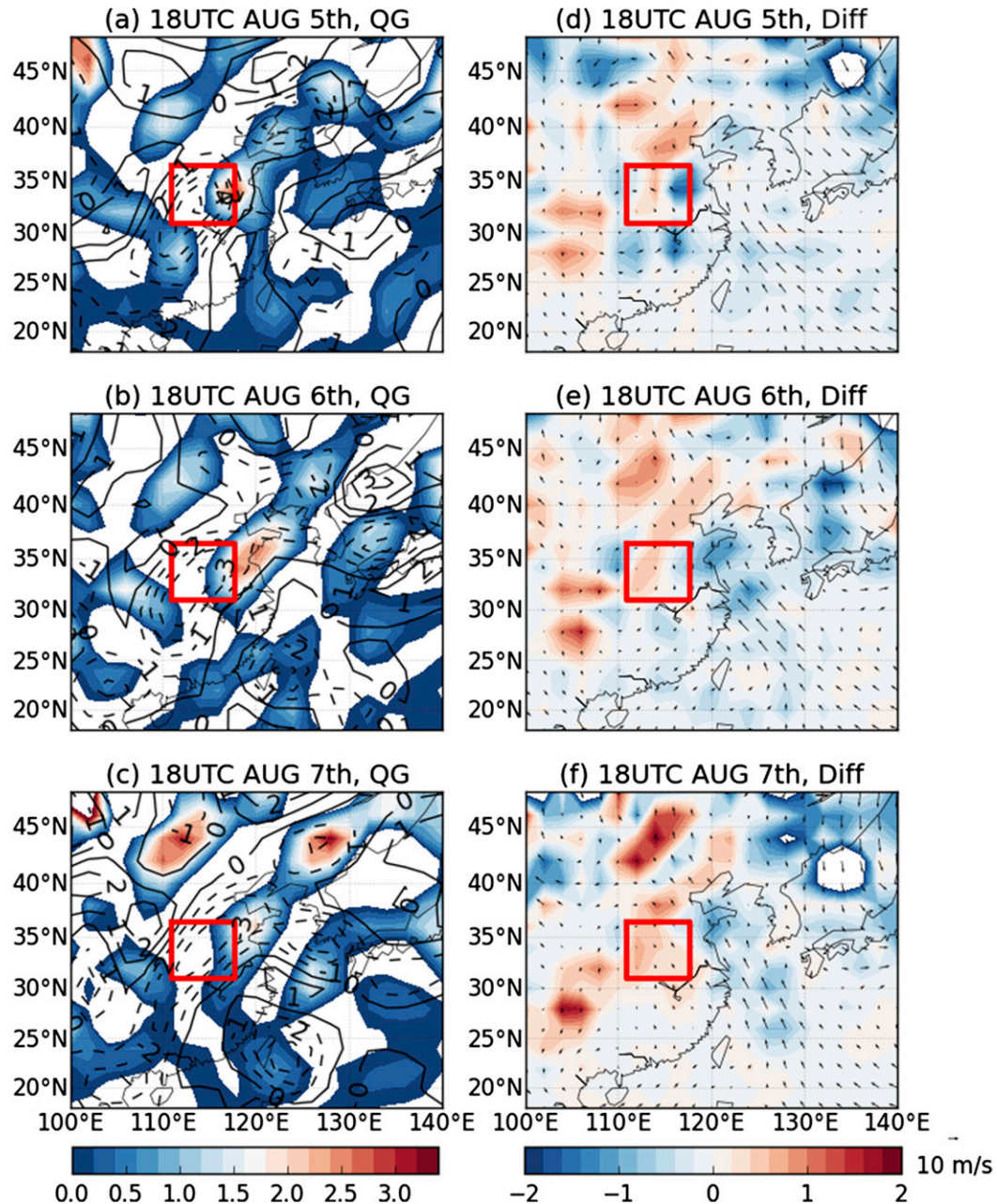FIG. 18. (left) Total QG forcing by summing terms A and B on the rhs of the QG omega equation (10–12 Pa m^{-2} s^{-1}; shaded, only positive values are plotted) and vertical wind at 700 hPa (10^{-1} Pa s^{-1}; contours, positive values referring to downward motion are in solid contours, negative values for upward motion are in dashed contours; contour interval is 0.1 Pa s^{-1}). (right) Relative importance of vorticity advection (term A) and thermal advection (term B) (10–12 Pa m^{-2} s^{-1}; shaded, positive values indicate dominance of vorticity advection, negative values indicate dominance of thermal advection) and horizontal wind (m s^{-1}; vectors) for 900 hPa at (a),(d) 1800 UTC 5 Aug; (b),(e) 1800 UTC 6 Aug; and (c),(f) 1800 UTC 7 Aug 1975. The red box outlines the spatial extent of central China.

side is the differential advection of geostrophic absolute vorticity by the geostrophic wind and the second term (term B) is the horizontal Laplacian of the thermal advection by the geostrophic advection. We examined the forcing for the vertical motion at 700 hPa. Term A was computed between 1000 and 500 hPa, and term B was evaluated at 700 hPa. Positive (negative) forcing summed from the two terms indicates upward (downward) motion.
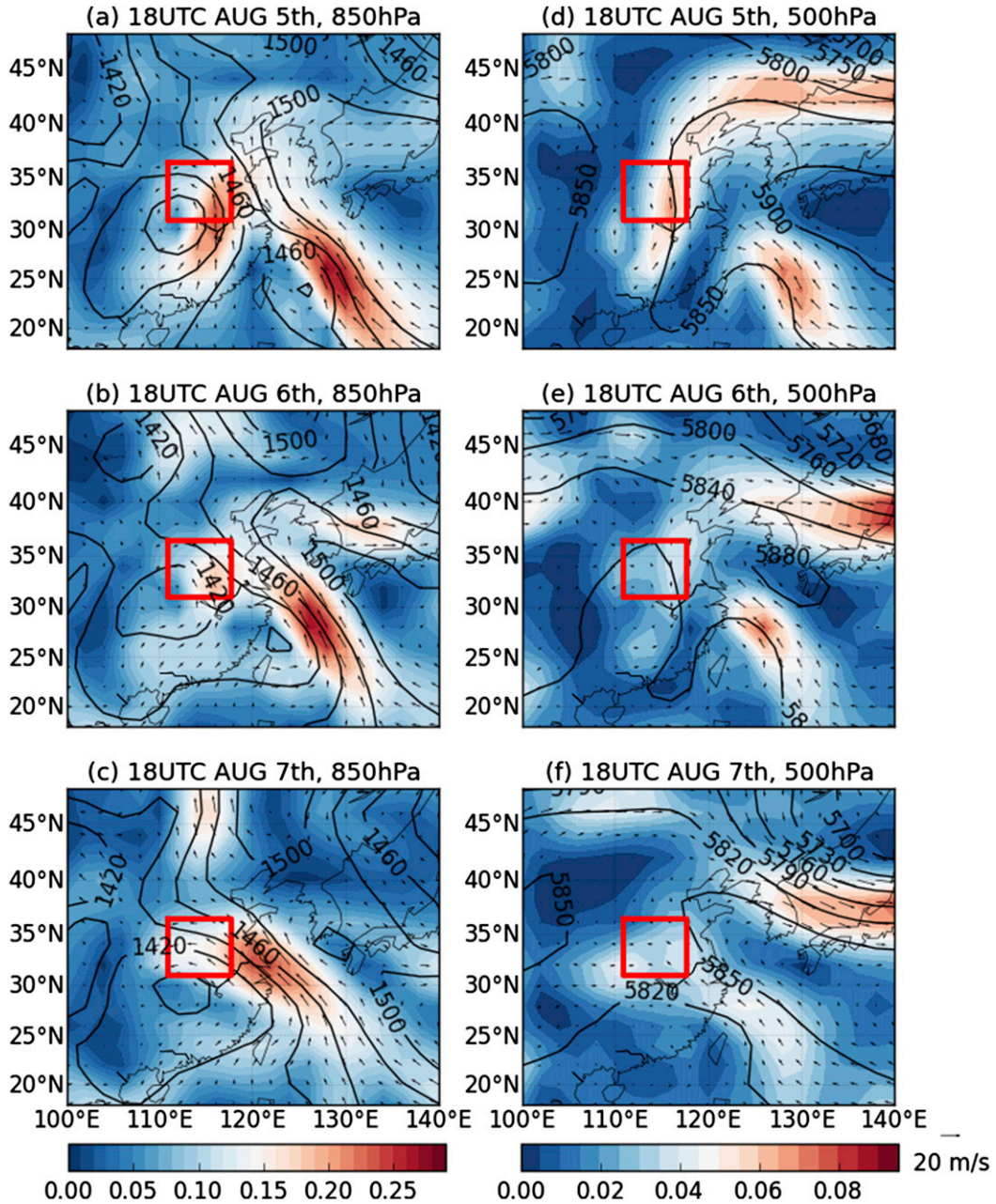
FIG. 19. Geopotential height (gpm; contours), wind field (m s^{-1}; vectors), and instantaneous water flux (kg kg^{-1} m s^{-1}; shaded) for (left) 850 and (right) 500 hPa at (a),(d) 1800 UTC 5 Aug; (b),(e) 1800 UTC 6 Aug; (c),(f) 1800 UTC 7 Aug 1975. The red box outlines the spatial extent of central China.

The total forcing at 700 hPa is generally consistent with the upward motion even though there are certain deviations of their maximum centers (Figs. 18a–c). The deviations might be related to other possible lifting mechanisms such as orographic lifting (see, e.g., Gao et al. 2009). The consistency of total forcing and upward motion indicates that synoptic forcing contributed to the heavy rainfall on 5–7 August 1975.

Figures 18d–f also show the relative dominance of vorticity and thermal advection (based on the difference between the absolute values of terms A and B in the QG omega equation) during the 3-day period. Positive (negative) values indicate that the vorticity (thermal) advection is the dominant factor. The QG synoptic forcing for upward motion over the central China region is predominantly due to thermal advection. There is a
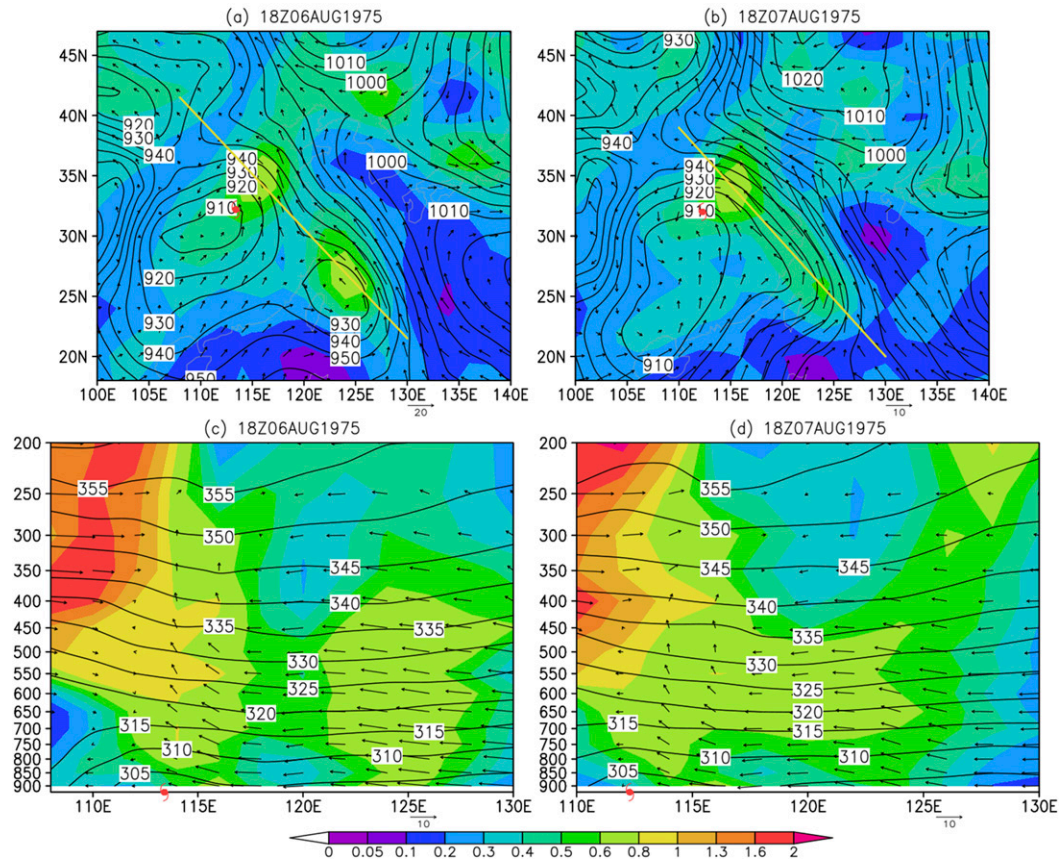
FIG. 20. (top) PV ($10–6$ K kg^{-1} m^2 s^{-1}; shaded), geopotential height (gpm; contours, contour interval is 10 gpm), and horizontal wind (m s^{-1}; vectors) at 900 hPa. (bottom) Cross sections of PV ($10–6$ K kg^{-1} m^2 s^{-1}; shaded), wind (m s^{-1}; vectors), and potential temperature (K; contours, contour interval is 5 K) at (a),(c) 1800 UTC 6 Aug and (b),(d) 1800 UTC 7 Aug 1975. The locations of the cross sections are represented as yellow lines in the top.

noticeable "plume" of thermal advection dominance located over northeastern Taiwan toward central China, following the strong horizontal wind vectors on 5–7 August (Figs. 18d–f). Analyses based on the QG omega equation suggest that warm air advection plays an important role in synoptic-scale vertical motion.

b. Interaction with the subsequent tropical depression

A key feature of the August 1975 flood was the interaction of Typhoon Nina with a second system (Fig. 19), a tropical depression that initiated 2 days after Nina made landfall on mainland China. The second system was recorded as Tropical Depression 05W (TD-05W) in the historical IBTrACS. At 1800 UTC 5 August, the 850-hPa height contour of 1460 gpm, which is generally the outer boundary of the west Pacific subtropical high, extended in a northwesterly direction into mainland China. Two corridors of strong water vapor flux (as represented by instantaneous water flux) were collocated with the two low pressure systems (Fig. 19a). Enhanced

water vapor flux is distributed continuously along the 500-hPa height contour of 5850 gpm (Fig. 19d). Another section of the 5850-gpm contour is distributed over inland China, which is a western portion of the subtropical high.

TD-05W moved closer to Nina on 6 August along the contour of 1460 gpm at 850 hPa. There was also an intensifying high pressure region to the north of the domain (around 40°–45°N) on 6 August, as reflected in the southward extension of the 1460-gpm contour (at 850 hPa; Fig. 19b). The lower section of the 1460-gpm contour (850 hPa) retreated because of this intensification. As a result, the orientation of the 1460-gpm contour (850 hPa) shifted westward, which favored direct water vapor flux associated with TD-05W into the circulation of Nina (Fig. 19b). At 1800 UTC 6 August, the contours of 5850 gpm (at 500 hPa) on the eastern section connected with the western section, forming an east–west-oriented barrier (Fig. 19e). Blocking by the high pressure barrier resulted in small net motion of Typhoon Nina, beginning on 6 August.

The high pressure region (as identified by the contour of 1460 gpm at 850 hPa to the north of the domain) continued to intensify into 7 August. At 1800 UTC 7 August, TD-05W merged into the circulation of Nina. The merged system established an exceptionally strong transport of water vapor from the Pacific Ocean directly into the storm region over Henan Province. The corridor of elevated water vapor transport is responsible for the increased water convergence as identified in section 4 and played a dominant role for the enhanced rain rate on 7 August. This is consistent with the dominant role of warm air advection in the synoptic-scale vertical motion based on the QG theory (see above analyses and Fig. 18 for details).

The dynamic and thermodynamic processes of the merger are well illustrated based on potential vorticity (PV) analyses (see, e.g., Hoskins et al. 1985; Atallah and Bosart 2003; Atallah et al. 2007). As seen in Fig. 20 at 1800 UTC 6 August, positive PV anomalies connected Nina and TD-05W, indicating the beginning of the merger process, even though the two storms maintained separate warm cores. At 1800 UTC 7 August, the two cores merged into a single core. The influx of positive PV anomalies into Nina maintained its circulation structure. The subtropical high split over land during 7 August (Fig. 19f). After a blocking period of more than 20 h, Typhoon Nina was steered to the southwest by the western part of the split subtropical high after 7 August, as reflected by southwestward shift of typhoon track in Fig. 6. The merger with TD-05W maintained the vortex structure of Typhoon Nina (Fig. 20), extending the period of heavy rainfall over the flood region into 7 August.

Mean profiles of water vapor flux (Fig. 21) show maximum flux on 7 August over the 3-day period and a vertical concentration between 1000 and 800 hPa. The pattern of low-level water vapor transport was favorable for creating a convectively unstable environment by initiating strong low-level convergence (as discussed in a previous section; see also Frank et al. 1999; Bao et al. 2015).

c. Backward trajectories of water vapor

We tracked the low-level water vapor using LAGRANTO [see Sprenger and Wernli (2015) for details] based on WRF-simulated fields (the outer domain). Backward trajectories of the water vapor initiating from the beginnings of the heaviest rain pulse during the 3-day period of 5–7 August 1975 illustrate the evolving water vapor transport (Fig. 22). Starting positions of backward tracking were initialized within the red box in Fig. 22 (the central China domain). We chose starting positions (within the domain) that are spaced by 0.2° (approximate 20 km) horizontally at a fixed vertical level of 900 hPa (identified as the moistest layer in Fig. 21). There are 676
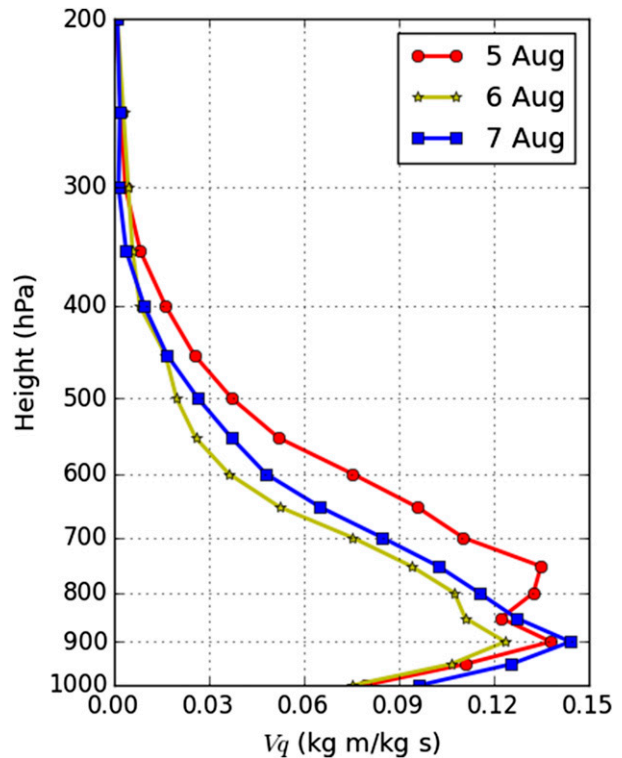

FIG. 21. Mean profiles of water vapor flux over the storm region on 5–7 Aug 1975.

trajectories used for the backward tracking. The backward trajectories on 5 August are sparsely distributed over the continent with no dominant sources (Fig. 22a), but become concentrated on 6 August due to the westward shift of the 1460-gpm contour at 850 hPa (Fig. 22b). On 7 August, the dominant trajectories were distributed across the continent and directly linked to the South China Sea (Fig. 22c), mostly due to the merger of TD-05W into Nina, which forms a strong water vapor conveyor belt. Air parcels were transported from the South China Sea into the rainfall region. Mean specific humidity along these trajectories is about $0.016 \, \text{kg kg}^{-1}$ (figure not shown).

6. Climatological context

In this section, we place the large-scale environment for the August 1975 flood into a climatological context based on analyses of 20CR fields. The mean geopotential height and wind field at 850 hPa during the period from 1200 UTC 31 July to 0000 UTC 8 August illustrates key features of the storm setting (Fig. 23a). The Western North Pacific Subtropical High (WNPH) is located around 40°N, 160°W, with its outer boundary (the contour of 1460 gpm) extending northwestward into northern China. The low-level transport of water vapor originated
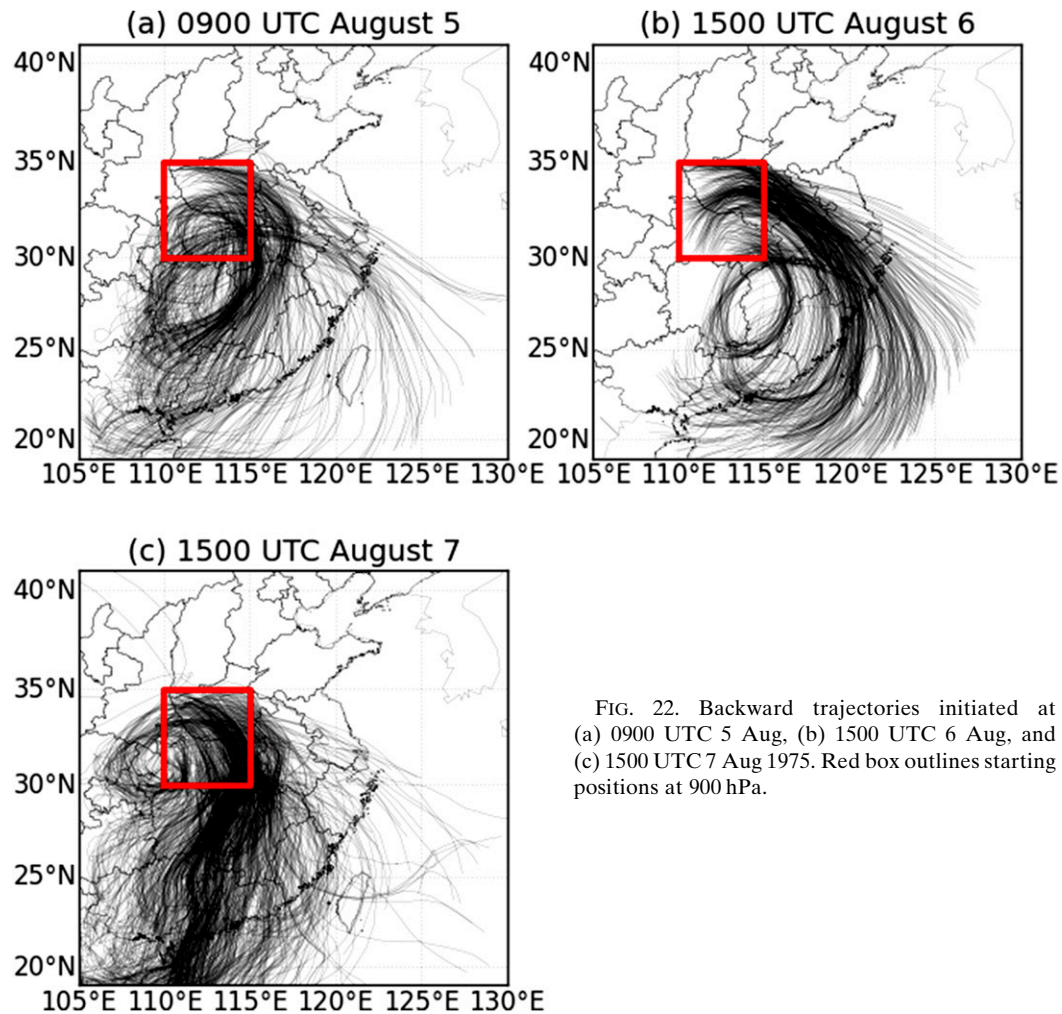
FIG. 22. Backward trajectories initiated at (a) 0900 UTC 5 Aug, (b) 1500 UTC 6 Aug, and (c) 1500 UTC 7 Aug 1975. Red box outlines starting positions at 900 hPa.

from the Bay of Bengal (via the South China Sea) and the Pacific Ocean confluence along the outer boundary of WNPH. Anomalies of averaged geopotential height at 850 hPa highlight significantly stronger WNPH than normal during the August 1975 flood period (with respect to the same period through the years of 1951–2013; Fig. 23b). A positive anomaly (higher by 30 gpm) of geopotential height at 850 hPa with west-to-east orientation was positioned over northern China (the high pressure barrier discussed earlier). The anomalously strong WNPH enhanced low-level wind speed by more than $10 \, \mathrm{m \, s^{-1}}$. The extreme rainfall region is located downstream of the enhanced low-level winds. The strong positive anomaly of low-level winds provides further evidence of the exceptional water vapor transport for the August 1975 flood over central China.

The small net storm motion during the critical period of heavy rainfall is linked to the blocking pattern highlighted in the mean geopotential height at 500 hPa. A blocking high, accompanied by an intensified westerly ridge, developed over the northern China region and extended to 50°N (Fig. 24a). The blocking high cut off the northward track of Nina. Instead of continuing to move northward, Nina remained stationary for more than 20 h over central China. This anomalous motion was responsible for initiating unprecedented rainfall and flooding over central China.

The integrated vapor transport (Fig. 25) was calculated from 1000 to 275 hPa (e.g., Lavers and Villarini 2013). Peak values of integrated vapor transport exceeded $1000 \, \mathrm{kg \, m^{-1} \, s^{-1}}$. The strong positive anomaly of about $350 \, \mathrm{kg \, m^{-1} \, s^{-1}}$ was concentrated along the outer boundary of the WNPH, highlighting the exceptional water vapor transport of this extreme rainfall event. Previous studies identified atmospheric rivers as important agents of extreme rainfall and flooding (see, e.g., Ralph et al. 2006; Lavers and Villarini 2013; Lu et al. 2013). Understanding the variability of
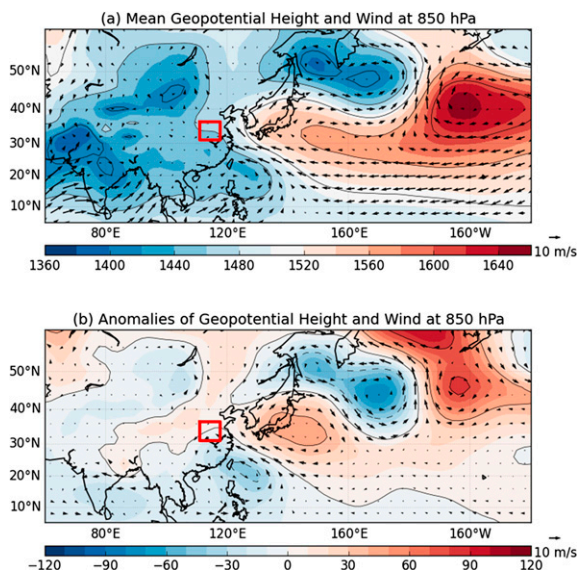
FIG. 23. (a) Mean geopotential height (gpm; shaded and contours) and wind field (m s^{-1}; vectors) at 850 hPa during the August 1975 flood period (from 1200 UTC 31 Jul to 0000 UTC 8 Aug 1975). (b) Anomalies of mean geopotential height (gpm; shaded and contours) and wind (m s^{-1}; vectors) at 850 hPa with respect to the same period all through the years of 1951–2013. The red box outlines the spatial extent of central China.

FIG. 24. As in Fig. 23, but for 500 hPa.

atmospheric rivers is also critical to extreme rainfall and flooding over mainland China (see also Zhou and Yu 2005; Simmonds et al. 1999).

The August 1975 flood reflects complex interactions of multiple physical processes at different temporal and spatial scales. We summarized the key features of extreme rainfall mechanisms for the flood event in Fig. 26. In this study, we do not draw sharp conclusions on the relative importance of these factors, but note that each serves as an element in establishing Typhoon Nina as one of most destructive flood agents in world history.

7. Summary and conclusions

In this study, we examined Typhoon Nina and the August 1975 flood over central China based on analyses of rainfall and streamflow observations and through analyses of downscaling simulations with the WRF Model driven by 20CR fields. Analyses of 20CR fields were used to provide a climatological context for Typhoon Nina. The major findings of this paper are as follows:

1) The August 1975 flood over central China was one of the most destructive floods over China, and flood magnitudes are comparable to the largest rainfall–runoff floods over the world. The peak discharge of
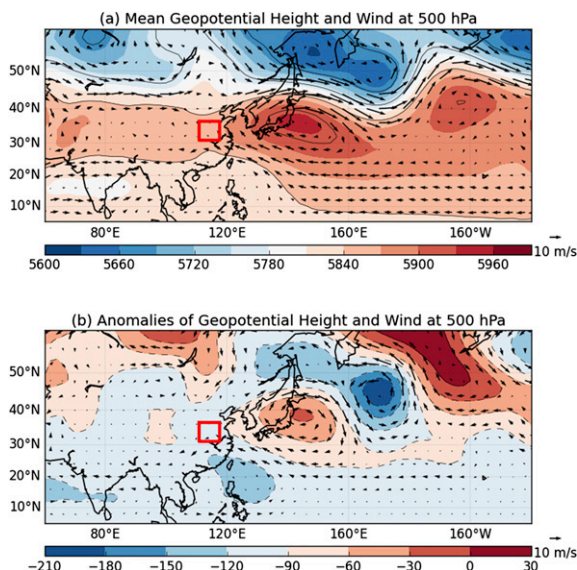
the Ru River of 13 000 m^3 s^{-1} at a drainage area of 760 km^2 is on the world envelope curve of flood peaks and resulted in catastrophic failure of the Banqiao Dam. The failures of Banqiao and Shimantan Dams were largely responsible for 26 000 direct fatalities and 100 000 additional fatalities from famine and disease.

2) Catastrophic flooding in the Henan Province of central China in 1975 was the product of extreme rainfall during a 3-day period extending from 5 through 7 August 1975. Measured rainfall accumulations during the 3-day period exceeded 1000 mm at eight rain gauge stations, with a maximum 3-day accumulation of 1605 mm at the Linzhuang station, just north of Banqiao Dam. The most exceptional consequences of Typhoon Nina were linked to catastrophic rainfall on 7 August in a relatively small area around Banqiao.
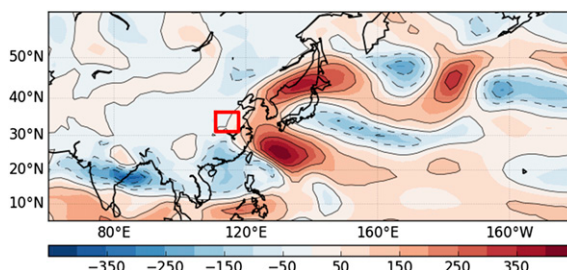

FIG. 25. Anomalies of integrated water vapor (kg m^{-1} s^{-1}) from 1200 UTC 31 Jul to 0000 UTC 8 Aug 1975, with respect to the same period all through the years of 1951–2013. The red box outlines the spatial extent of central China.
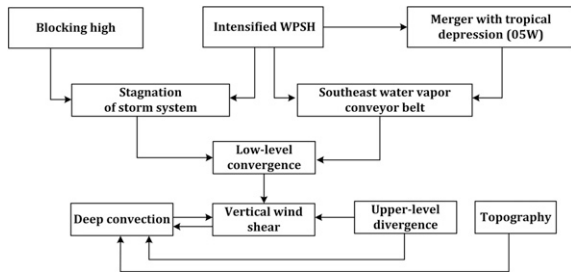
FIG. 26. Schematic for the physical mechanisms of extreme rainfall for the August 1975 flood over central China.

3) The structure of extreme rainfall in central China changed markedly over the period of 5–7 August. Downscaling simulations with WRF capture important elements of the evolution of Typhoon Nina and are used to provide insights to changing properties of rainfall. The WRF simulations underestimated rainfall intensity, limiting the inferences that can be drawn. Rainfall on 5 August was related to the interactions of outer rainbands of Nina with a weak warm front. Heavy rainfall on 5 August was also associated with mergers of storm elements and repeated tracking of storm elements over localized regions. Rainfall on 6 August assumed a pronounced asymmetric structure, with a concentration of heavy rainfall in the right-rear quadrant of the storm system, linked to the role of vertical wind shear and asymmetric mass flux. Rainfall magnitudes increased on 7 August, and the multiple rainbands on 6 August were replaced by a single major rainband with a south–north orientation.

4) Blocking played a central role in controlling the duration and magnitude of extreme rainfall in central China from Typhoon Nina. The large-scale environment for the August 1975 flood was characterized by an anomalously strong WNPH and the transition of the western margin of the ridge to northeastern Asia. Typhoon Nina remained stationary upstream of the blocking region, resulting in the small net storm motion and persistent, extreme rainfall over southern Henan province for 3 days.

5) The interaction of Typhoon Nina and TD-05W was an important feature of the August 1975 flood. The tropical depression enhanced the transport of warm, moist water vapor from the tropical ocean into the cyclonic system. The merger of TD-05W and Typhoon Nina established a period of anomalously strong low-level water vapor transport preceding and during the period of catastrophic rainfall on 7 August. Analyses based on quasigeostrophic omega equation identified the prominent role of warm air advection in producing synoptic-scale uplift.

6) Extreme rainfall for the August 1975 flood was linked to anomalously large water vapor transport from the west Pacific Ocean. The water vapor transport into the extreme rainfall region was characterized by vertical profiles of water flux concentrated over low vertical levels (1000–800 hPa), indicating the critical role of low-level water transport in producing extreme rainfall and flooding over mainland China. Backward tracking of low-level water vapor identified South China Sea as a dominant source region of water vapor for the August 1975 flood over central China.

Hydrometeorological analyses provide an important pathway to address problems of engineering design for flood-control structures. The August 1975 flood demonstrated a combination of favorable ''ingredients'' for extreme rainfall and flooding and organized them into a favorable space and time as well. Analyses of this type have played a central role in developing procedures for implementing PMP computations (see, e.g., Myers 1969). We need to realize, however, that events like the August 1975 flood may reflect a unique combination of rare ingredients and not a broader set of patterns that broadly contribute to the historical extremes of rainfall and flooding. Characterizing the ''nature'' of the upper tail of rainfall and flood distributions remains a challenging problem, both from a theoretical perspective and from the perspective of developing effective procedures for addressing flood hazards. The analytical framework presented in this study provided a promising approach to examine the temporal and spatial variation of extreme rainfall from major flood producing storms in the historical record, and, ultimately, in characterizing the nature of the upper tail of extreme rainfall.

REFERENCES

Atallah, E. H., and L. F. Bosart, 2003: The extratropical transition and precipitation distribution of Hurricane Floyd (1999). *Mon. Wea. Rev.*, **131**, 1063–1081, doi:10.1175/1520-0493(2003)131<1063:TETAPD>2.0.CO;2.

——, ——, and A. R. Aiyyer, 2007: Precipitation distribution associated with landfalling tropical cyclones over the eastern United States. *Mon. Wea. Rev.*, **135**, 2185–2206, doi:10.1175/MWR3382.1.

Bao, X., and Coauthors, 2015: Diagnostics for an extreme rain event near Shanghai during the landfall of Typhoon Fitow (2013). *Mon. Wea. Rev.*, **143**, 3377–3405, doi:10.1175/MWR-D-14-00241.1.

Changnon, S. A., R. G. Semonin, and F. A. Huff, 1976: A hypothesis for urban rainfall anomalies. *J. Appl. Meteor.*, **15**, 544–560, doi:10.1175/1520-0450(1976)015<0544:AHFURA>2.0.CO;2.

Chen, S. S., J. A. Knaff, and F. D. Marks, 2006: Effects of vertical wind shear and storm motion on tropical cyclone rainfall asymmetries deduced from TRMM. *Mon. Wea. Rev.*, **134**, 3190–3208, doi:10.1175/MWR3245.1.

Chen, X., and F. Hossain, 2016: Revisiting extreme storms of the past 100 years for future safety of large water management infrastructures. *Earth's Future*, **4**, 306–322, doi:10.1002/2016EF000368.

Colle, B. A., 2003: Numerical simulations of the extratropical transition of Floyd (1999): Structural evolution and responsible mechanisms for the heavy rainfall over the northeast United States. *Mon. Wea. Rev.*, **131**, 2905–2926, doi:10.1175/1520-0493(2003)131<2905:NSOTET>2.0.CO;2.

Compo, G. P., and Coauthors, 2011: The Twentieth Century Reanalysis project. *Quart. J. Roy. Meteor. Soc.*, **137**, 1–28, doi:10.1002/qj.776.

Corbosiero, K. L., and J. Molinari, 2002: The effects of vertical wind shear on the distribution of convection in tropical cyclones. *Mon. Wea. Rev.*, **130**, 2110–2123, doi:10.1175/1520-0493(2002)130<2110:TEOVWS>2.0.CO;2.

——, and ——, 2003: The relationship between storm motion, vertical wind shear, and convective asymmetries in tropical cyclones. *J. Atmos. Sci.*, **60**, 366–376, doi:10.1175/1520-0469(2003)060<0366:TRBSMV>2.0.CO;2.

Costa, J. E., 1987: A comparison of the largest rainfall–runoff floods in the United States with those of the People's Republic of China and the world. *J. Hydrol.*, **96**, 101–115, doi:10.1016/0022-1694(87)90146-6.

Dai, Q., 1998: *The River Dragon Has Come! The Three Gorges Dam and the Fate of China's Yangtze River and Its People.* J. G. Thibodeau and P. B. Williams, Eds., Routledge, 270 pp.

Dalrymple, T., 1960: Flood-frequency analyses. Manual of Hydrology: Part 3. Flood-flow techniques, USGS Water-Supply Paper 1543-A, 80 pp. [Available online at https://pubs.usgs.gov/wsp/1543a/report.pdf.]

Davis, C. A., and Coauthors, 2008a: Prediction of landfalling hurricanes with the advanced hurricane WRF Model. *Mon. Wea. Rev.*, **136**, 1990–2005, doi:10.1175/2007MWR2085.1.

——, S. C. Jones, and M. Riemer, 2008b: Hurricane vortex dynamics during Atlantic extratropical transition. *J. Atmos. Sci.*, **65**, 714–736, doi:10.1175/2007JAS2488.1.

Ding, Y. H., 2015: On the study of the unprecedented heavy rainfall in Henan Province during 4–8 August 1975: Review and assessment. *Acta Meteor. Sin.*, **73**, 411–424, doi:10.11676/qxxb2015.067.

——, and J. Y. Zhang, 2009: *Torrential Rains and Flashing Floods.* Meteorological Press, 290 pp.

Evans, J. L., and R. E. Hart, 2003: Objective indicators of the life cycle evolution of extratropical transition for Atlantic tropical cyclones. *Mon. Wea. Rev.*, **131**, 909–925, doi:10.1175/1520-0493(2003)131<0909:OIOTLC>2.0.CO;2.

Fish, E., 2013: The forgotten legacy of the Banqiao Dam collapse. *Economic Observer*, 8 February. [Available online at http://www.eeo.com.cn/ens/2013/0208/240078.shtml.]

Frank, W. M., W. M. Frank, E. A. Ritchie, and E. A. Ritchie, 1999: Effects of environmental flow upon tropical cyclone structure. *Mon. Wea. Rev.*, **127**, 2044–2061, doi:10.1175/1520-0493(1999)127<2044:EOEFUT>2.0.CO;2.

Fu, A., 2005: Problems of design floods for Shimantan and Banqiao reservoir. *China Water Resour.*, **16**, 39–41.

Fu, D., and X. Guo, 2012: A cloud-resolving simulation study on the merging processes and effects of topography and environmental winds. *J. Atmos. Sci.*, **69**, 1232–1249, doi:10.1175/JAS-D-11-049.1.

Gao, S., and X. Li, 2008: Precipitation efficiency. *Cloud-Resolving Modeling of Convective Processes.* Springer, 137–146.

——, Z. Meng, F. Zhang, and L. F. Bosart, 2009: Observational analysis of heavy rainfall mechanisms associated with severe Tropical Storm Bilis (2006) after its landfall. *Mon. Wea. Rev.*, **137**, 1881–1897, doi:10.1175/2008MWR2669.1.

Gupta, H. V., C. Perrin, G. Blöschl, A. Montanari, R. Kumar, M. Clark, and V. Andréassian, 2014: Large-sample hydrology: A need to balance depth with breadth. *Hydrol. Earth Syst. Sci.*, **18**, 463–477, doi:10.5194/hess-18-463-2014.

Hamada, A., Y. N. Takayabu, C. Liu, and E. J. Zipser, 2015: Weak linkage between the heaviest rainfall and tallest storms. *Nat. Commun.*, **6**, 6213, doi:10.1038/ncomms7213.

Hart, R. E., 2003: A cyclone phase space derived from thermal wind and thermal asymmetry. *Mon. Wea. Rev.*, **131**, 585–616, doi:10.1175/1520-0493(2003)131<0585:ACPSDF>2.0.CO;2.

Hoskins, B. J., M. E. McIntyre, and A. W. Robertson, 1985: On the use and significance of isentropic potential vorticity maps. *Quart. J. Roy. Meteor. Soc.*, **111**, 877–946, doi:10.1002/qj.49711147002.

Hu, M., and C. Luo, 1992: *Historical Floods of China.* China Bookstore Publishing House, 727 pp.

Huang, H. L., M. J. Yang, and C. H. Sui, 2014: Water budget and precipitation efficiency of Typhoon Morakot (2009). *J. Atmos. Sci.*, **71**, 112–129, doi:10.1175/JAS-D-13-053.1.

Jankov, I., W. A. Gallus, M. Segal, B. Shaw, and S. E. Koch, 2005: The impact of different WRF Model physical parameterizations and their interactions on warm season MCS rainfall. *Wea. Forecasting*, **20**, 1048–1060, doi:10.1175/WAF888.1.

Jones, S. C., and Coauthors, 2003: The extratropical transition of tropical cyclones: Forecast challenges, current understanding, and future directions. *Wea. Forecasting*, **18**, 1052–1092, doi:10.1175/1520-0434(2003)018<1052:TETOTC>2.0.CO;2.

Khain, A., B. Lynn, and J. Shpund, 2016: High resolution WRF simulations of Hurricane Irene: Sensitivity to aerosols and choice of microphysical schemes. *Atmos. Res.*, **167**, 129–145, doi:10.1016/j.atmosres.2015.07.014.

Knapp, K. R., M. C. Kruk, D. H. Levinson, H. J. Diamond, and C. J. Neumann, 2010: The International Best Track Archive for Climate Stewardship (IBTrACS). *Bull. Amer. Meteor. Soc.*, **91**, 363–376, doi:10.1175/2009BAMS2755.1.

Knutson, T. R., and Coauthors, 2013: Dynamical downscaling projections of twenty-first-century Atlantic hurricane activity: CMIP3 and CMIP5 model-based scenarios. *J. Climate*, **26**, 6591–6617, doi:10.1175/JCLI-D-12-00539.1.

Lall, U., and L. R. Beard, 1982: Estimation of Pearson type 3 moments. *Water Resour. Res.*, **18**, 1563–1569, doi:10.1029/WR018i005p01563.

Lavers, D. A., and G. Villarini, 2013: The nexus between atmospheric rivers and extreme precipitation across Europe. *Geophys. Res. Lett.*, **40**, 3259–3264, doi:10.1002/grl.50636.

Li, C. Q., G. A. Wang, and R. R. Li, 2013: Maximum observed floods in China. *Hydrol. Sci. J.*, **58**, 728–735, doi:10.1080/02626667.2013.772299.

Li, L., W. Li, and J. Jin, 2014: Improvements in WRF simulation skills of southeastern United States summer rainfall: Physical parameterization and horizontal resolution. *Climate Dyn.*, **43**, 2077–2091, doi:10.1007/s00382-013-2031-2.

Liu, M. F., and J. A. Smith, 2016: Extreme rainfall from landfalling tropical cyclones in the eastern United States: Hurricane Irene (2011). *J. Hydrometeor.*, **17**, 2883–2904, doi:10.1175/JHM-D-16-0072.1.

Lu, M., U. Lall, A. Schwartz, and H. Kwon, 2013: Precipitation predictability associated with tropical moisture exports and circulation patterns for a major flood in France in 1995. *Water Resour. Res.*, **49**, 6381–6392, doi:10.1002/wrcr.20512.

Luo, C., and G. Shen, 1987: Catalogue of maximum floods and its geographic attributes. *J. Chinese Hydrol.*, **5**, 5–10.

Myers, V. A., 1969: The estimation of extreme precipitation as the basis for design floods: Resume of practice in the United States, *IAHS Publ.*, **84–85**, 84–101. [Available online at http://iahs.info/uploads/dms/084011.pdf.]

NOAA, 2007: The worst natural disasters by death toll. Accessed November 2015. [Available online at http://docs.lib.noaa.gov/noaa_documents/NOAA_related_docs/death_toll_natural_disasters.pdf.]

Ping, F., Z. Luo, X. Tang, and L. Hu, 2014: A simulation of the merger of convective clouds in the torrential rainfalls associated with the Meiyu front. *Meteor. Atmos. Phys.*, **123**, 51–65, doi:10.1007/s00703-013-0294-0.

Ralph, F. M., P. J. Neiman, G. A. Wick, S. I. Gutman, M. D. Dettinger, D. R. Cayan, and A. B. White, 2006: Flooding on California's Russian River: Role of atmospheric rivers. *Geophys. Res. Lett.*, **33**, L13801, doi:10.1029/2006GL026689.

Schreck, C., and Coauthors, Eds., 2013: The Climate Data Guide: IBTrACS: Tropical cyclone best track data. NCAR/UCAR, accessed November 2015. [Available online at https://climatedataguide.ucar.edu/climate-data/ibtracs-tropical-cyclone-best-track-data.]

Simmonds, I., D. Bi, and P. Hope, 1999: Atmospheric water vapor flux and its association with rainfall over China in summer. *J. Climate*, **12**, 1353–1367, doi:10.1175/1520-0442(1999)012<1353:AWVFAI>2.0.CO;2.

Skamarock, W. C., and Coauthors, 2008: A description of the Advanced Research WRF version 3. NCAR Tech. Note NCAR/TN-475+STR, 113 pp., doi:10.5065/D68S4MVH.

Smith, J. A., and M. L. Baeck, 2015: "Prophetic vision, vivid imagination": The 1927 Mississippi River flood. *Water Resour. Res.*, **51**, 9964–9994, doi:10.1002/2015WR017927.

Special Research Team for the "75.8" heavy rainstorm, 1977a: Preliminary analysis of cause of the "75.8" heavy rainstorm Part I. *Meteor. Monogr.*, **3**, 3–5.

——, 1977b: Preliminary analysis of causes of the "75.8" heavy rainstorm Part II. *Meteor. Monogr.*, **3**, 6–8.

Sprenger, M., and H. Wernli, 2015: The LAGRANTO Lagrangian analysis tool—Version 2.0. *Geosci. Model Dev.*, **8**, 2569–2586, doi:10.5194/gmd-8-2569-2015.

Sui, C. H., X. Li, and M. J. Yang, 2007: On the definition of precipitation efficiency. *J. Atmos. Sci.*, **64**, 4506–4513, doi:10.1175/2007JAS2332.1.

Teegavarapu, R. S. V., 2013: *Floods in a Changing Climate: Extreme Precipitation.* Cambridge University Press, 285 pp.

Trenberth, K. E., 1978: On the interpretation of the diagnostic quasi-geostrophic omega equation. *Mon. Wea. Rev.*, **106**, 131–137, doi:10.1175/1520-0493(1978)106<0131:OTIOTD>2.0.CO;2.

Villarini, G., and J. A. Smith, 2010: Flood peak distributions for the eastern United States. *Water Resour. Res.*, **46**, W06504, doi:10.1029/2009WR008395.

Wang, G., 2006: The main cause and lesson of "August 1975" dam-breaking floods in the Huaihe River. *Sci. Technol. Rev.*, **24**, 72–77.

Wang, Y., 2005: Recognition of hydrological rules from the "75.8" flood. *China Water Resour.*, **16**, 42–44.

Wu, L., B. Wang, and S. Geng, 2005: Growing typhoon influence on East Asia. *Geophys. Res. Lett.*, **32**, L18703, doi:10.1029/2005GL022937.

Xie, B., and F. Zhang, 2012: Impacts of typhoon track and island topography on the heavy rainfalls in Taiwan associated with Morakot (2009). *Mon. Wea. Rev.*, **140**, 3379–3394, doi:10.1175/MWR-D-11-00240.1.

Yang, L., 2005: "75.8" flood and main lessons. *Zhihuai*, **8**, 13.

——, G. Villarini, J. A. Smith, F. Tian, and H. Hu, 2013: Changes in seasonal maximum daily precipitation in China over the period 1961–2006. *Int. J. Climatol.*, **33**, 1646–1657, doi:10.1002/joc.3539.

——, J. A. Smith, M. L. Baeck, D. Niyogi, and F. Tian, 2016: Structure and evolution of flash flood producing storms in a small urban watershed. *J. Geophys. Res. Atmos.*, **121**, 3139–3152, doi:10.1002/2015JD024478.

Zhang, S. Q., M. Zupanski, A. Y. Hou, X. Lin, and S. H. Cheung, 2013: Assimilation of precipitation-affected radiances in a cloud-resolving WRF ensemble data assimilation system. *Mon. Wea. Rev.*, **141**, 754–772, doi:10.1175/MWR-D-12-00055.1.

Zhou, T.-J., and R.-C. Yu, 2005: Atmospheric water vapor transport associated with typical anomalous summer rainfall patterns in China. *J. Geophys. Res.*, **110**, D08104, doi:10.1029/2004JD005413.